

MOCCA-SURVEY Database – I. Tidal disruption events of white dwarfs in globular clusters and young massive clusters

Ataru Tanikawa^{1*}, Mirek Giersz², Manuel Arca Sedda³

¹*Department of Earth Science and Astronomy, College of Arts and Sciences, The University of Tokyo, 3-8-1 Komaba, Meguro-ku, Tokyo 153-8902, Japan*

²*Nicolaus Copernicus Astronomical Centre, Polish Academy of Sciences, ul. Bartycka 18, PL-00-716 Warsaw, Poland*

³*Astronomisches Rechen-Institut, Zentrum für Astronomie der Universität Heidelberg, Mönchhofstr. 12-14, D-69120 Heidelberg, Germany*

Accepted XXX. Received YYY; in original form ZZZ

ABSTRACT

We exploit more than 1000 star cluster Monte Carlo models from the MOCCA-SURVEY Database I, to infer the local rate density of white dwarf (WD) tidal disruption events (TDEs) in globular clusters (GCs) and young massive clusters (YMCs). We suggest that the WD TDE rate for GCs and YMCs in the local universe is $\sim 90\text{--}500 \text{ yr}^{-1} \text{ Gpc}^{-3}$, with 90 % of WD TDEs occurring in GCs. The total WD TDE rate density is $\sim 9\text{--}50$ times larger than estimated before. Our results show that thermonuclear explosions induced by WD TDEs can be observed at a rate of $\sim 100\text{--}550 \text{ yr}^{-1}$ by the next generation optical surveys, such as the Legacy Survey of Space & Time by the Vera C. Rubin Observatory. We also find that massive WDs are preferentially disrupted due to mass segregation, and that 20 % of exploding WDs have $\geq 1.0 M_{\odot}$ despite of the small population of such WDs.

Key words: stars: white dwarfs – globular clusters: general

1 INTRODUCTION

A star closely approaching a black hole (BH) can be torn apart by the gravitational pull and undergo a so-called tidal disruption event (TDE) (for recent reviews, see Komossa 2015; Stone et al. 2019; Rossi et al. 2020). A subclass of TDEs involves the disruption of a white dwarf (WD), thus being referred to as WD TDE (see review by Maguire et al. 2020).

WD TDEs can be a promising target of multi-messenger astronomy. As electromagnetic (EM) sources, they have been suggested as the origin of high-energy transients associated with gamma-ray emissions (Krolik & Piran 2011; Levan et al. 2014; MacLeod et al. 2014; Ioka et al. 2016). BHs accrete WD debris, and can accompany X-ray flares (Jonker et al. 2013; Shen 2019), and optical/ultraviolet transients (Clausen & Eracleous 2011). When a WD deeply penetrates within the tidal radius, it can experience thermonuclear explosion, and can be observed as a subtype of type Ia supernovae (SNe Ia) (Luminet & Pichon 1989; Rosswog et al. 2008, 2009a; MacLeod et al. 2016a; Tanikawa et al. 2017; Tanikawa 2018a,b; Kawana et al. 2018, 2020; Anninos et al. 2018, 2019), or calcium-rich gap transients (Sell et al. 2015, 2018). Kuin et al. (2019) have claimed a WD TDE as the origin of a rapidly rising and luminous transient AT2018cow (Prentice et al. 2018). Aside from EM waves, WD TDEs should emit gravitational waves (GWs) just before WDs are disrupted (Sesana et al. 2008). Since WDs are much less compact than neutron stars and BHs, the GW frequency does not match with ground-based GW observatories, such as LIGO, Virgo, and KAGRA (LIGO Scientific Collaboration et al. 2015; Acernese et al. 2015; Kagra Collaboration

et al. 2019, respectively). LISA (Amaro-Seoane et al. 2017) may detect GW emissions from WD TDEs, if the WD TDEs occur in the local group (Rosswog et al. 2009a; Anninos et al. 2018). Arca Sedda et al. (2020) have shown that GW observatories with sensitivity at a decihertz frequency, such as ALIA and DECIGO (Mueller et al. 2019; Kawamura et al. 2011, respectively), can discover GWs of WD TDEs even in the high-redshift universe. Several studies have suggested that WD TDEs can be sources of ultra high-energy cosmic rays and neutrinos (Zhang et al. 2017; Alves Batista & Silk 2017; Biehl et al. 2018).

WD TDEs represent a powerful way to probe the mass range of intermediate-mass black holes (IMBHs), i.e. $10^2 - 10^4 M_{\odot}$ (Luminet & Pichon 1989; Rosswog et al. 2009b; Kawana et al. 2018). In fact, heavier IMBHs would directly swallow the WD, whilst lighter BHs would most likely penetrate the WD and form a variant of a Thorne-Zytkow object (TZO Thorne & Zytkow 1975). Even though IMBHs should be a key to solve the formation of massive BHs (MBHs) with $\geq 10^5 M_{\odot}$ (e.g. Rees 1984; Ebisuzaki et al. 2001; Volonteri 2012), a small number of IMBHs (or their promising candidates) have been discovered so far, such as M82 X-1 (Matsumoto et al. 2001), HLX-1 (Farrell et al. 2009), free-floating IMBH candidates observed in the Milky Way (MW) (Tanaka et al. 2014; Tanaka 2018; Takekawa et al. 2019, 2020), and the merger remnant of a binary BH GW190521 (Abbott et al. 2020a,b).

Until today, no conclusive WD TDE has been reported, although there are several candidates. This might owe to observational limits or more fundamental reasons intrinsically connected with the co-evolution of IMBHs and their stellar neighborhoods. Thus, it is crucial to construct a theoretical framework to compare with future observation surveys, like the one attainable with the Legacy Survey

* E-mail: tanikawa@ea.c.u-tokyo.ac.jp

of Space & Time (LSST) by the Vera C. Rubin Observatory (Ivezić et al. 2019). The observational features of a WD TDE are expected to largely depend on the WD and BH properties. On the one hand, accretion-driven flares are supposed to increase luminosity at increasing the BH mass, assuming Eddington-limited accretion. On the other hand, the WD composition, which determine the explosive mechanisms and the observational features, varies with its mass, so that from lighter to heavier WDs we have helium (He), carbon oxygen (CO), and oxygen-neon (ONe) WDs.

WD TDEs can happen in two types of stellar systems harboring IMBHs. The first type is represented by dwarf galaxies (Reines et al. 2013). They are expected to contain IMBHs, since they are on the extension line of the relation between MBHs and their host galaxies (Kormendy & Richstone 1995; Magorrian et al. 1998; Ferrarese & Merritt 2000; Kormendy & Ho 2013). The second type is represented by star clusters, such as globular clusters (GCs Jonker et al. 2012) and young massive clusters (YMCs Portegies Zwart et al. 2010). IMBHs' seeds and themselves are theoretically considered to form through repeated mergers of stars or stellar-mass BHs (e.g. Portegies Zwart et al. 2004; Giersz et al. 2015).

In this paper, we focus on WD TDEs in YMCs and GCs. Previous studies investigated the development of WD TDEs in numerical simulations of star clusters (Baumgardt et al. 2004a; MacLeod et al. 2016b). However, in the majority of these studies the IMBH was placed in the cluster center ab-initio, thus avoiding the complex phases affecting the IMBH seeding and growth. Here, we exploit the MOCCA-SURVEY Database I, a suite of 2000 Monte Carlo simulations representing star clusters with masses in the range $10^4 - 10^6 M_\odot$. These simulations couple dynamics and stellar evolution of single and binary stars, thus enabling us to closely follow the possible formation of an IMBH and development of a WD TDE. Moreover, the large amount of available MOCCA models permit us to dissect the properties of the BHs and WDs involved in a TDE. The MOCCA-SURVEY Database I have been already used widely to study star clusters from various points (Belloni et al. 2016, 2017, 2019; Askar et al. 2017a,b, 2018; Samsing et al. 2018; Arca Sedda et al. 2018, 2019; Morawski et al. 2018; Giersz et al. 2019a,b; Hong et al. 2020; Leveque et al. 2021).

This paper is structured as follows. In section 2, we introduce MOCCA-SURVEY Database I, and describe a method to calculate the total event rate of WD TDEs and its derivatives. In sections 3 and 4, we show the results, and compare the results with previous studies, respectively. In section 5, we discuss about detectability of WD TDEs, using our results. In section 6, we summarize this paper.

2 METHOD

We use MOCCA-SURVEY Database I in order to derive the event rate of WD TDEs in GCs and YMCs. Before we introduce the database, we briefly describe the MOCCA (MOnte Carlo Cluster simulAtor) code generating the database. MOCCA clusters have been generated thanks to MOCCA, a Monte Carlo code based on Hénon's implementation (Hénon 1971) to follow the dynamical evolution of star clusters, and includes improvements by Stodolkiewicz (1986) and Giersz et al. (2008, 2013). It can deal with single and binary star evolutions provided by Hurley et al. (2000) and Hurley et al. (2002), respectively. The MOCCA code contains the FEWBODY code (Fregeau et al. 2004) as a module in order to solve close encounters among single and binary stars by direct integration. The MOCCA code models galactic tidal fields with reference to the theory of potential escapers developed by Fukushima & Heggie (2000).

We present initial conditions and setup of the database in Table 1, where N is the initial total number of single and binary stars in a cluster, R_t and R_h are the initial tidal and half-mass radii of a cluster, W_0 is the initial concentration parameter of King's model (King 1966) adopted for the initial phase space distribution of each cluster, Z is the metallicity of a cluster, f_b is the initial binary fraction of a cluster, and N_{cl} is the number of clusters. A stellar initial mass function (IMF) in each cluster is Kroupa's IMF (Kroupa 2001) in which the minimum and maximum stellar masses are $0.08 M_\odot$ and $100 M_\odot$, respectively. We adopt the model of Belczynski et al. (2002) for supernova model. Supernova natal kick velocities for neutron stars (NSs) are drawn from a Maxwellian distribution with a dispersion of 265 km s^{-1} (Hobbs et al. 2005). BH natal kicks are modified by the mass fallback described by Belczynski et al. (2002). We select only models with BH natal kick modified by the mass fallback, and thus our sample is limited to about 1000 MOCCA models, as summarized in Table 1. Each cluster is embedded in an external tidal field by a point-mass galaxy with the flat rotation velocity, 220 km s^{-1} . According to the adopted galaxy model, several MOCCA clusters can be dragged to the galactic center via dynamical friction (Tremaine et al. 1975; Capuzzo-Dolcetta 1993; Gnedin et al. 2014; Arca-Sedda & Capuzzo-Dolcetta 2014), a feature that is not implemented in the MOCCA code. Therefore, we exclude from our analysis all clusters with a dynamical friction timescale $< 10 \text{ Gyr}$ (Arca Sedda et al. 2019). We do not account for these clusters to count the event rate of WD TDEs in the current GCs. In Table 1, we indicate with N_{cl} the number of clusters that survive to the dynamical friction drag. Leveque et al. (2021) have shown that these cluster models match pretty well the MW GC system. As YMCs, we select clusters with $N \leq 10^5$ and $Z = 0.02$ from the MOCCA models. This is because YMCs have at most $\sim 10^5 M_\odot$ and at least ~ 0.02 or Z_\odot (Portegies Zwart et al. 2010). In the following, we will thus consider MOCCA models as representative of the typical population of GCs and YMCs.

Figure 1 shows the cumulative distribution function (CDF) of the maximum BH masses calculated after 12 Gyr in all the examined models. About 19, 16 and 4.8 % of them contain BHs with $> 10^2$, $> 10^3$, and $> 10^4 M_\odot$ BHs, respectively. We set $10^2 M_\odot$ as the threshold to distinguish between stellar mass BHs and IMBHs. According to this definition, the IMBH occupation fraction in our models is $f_{BH,GC} = 0.19$. We note that this represents the most optimistic case, as here we neglect the effect of GW recoil kick imparted on BH merger remnants and the impact of the IMBH formation scenario. We discuss a pessimistic scenario that accounts for these features in Appendix C. The CDFs are not sensitive to metallicity (Z) and initial binary fraction (f_b) as seen in the top and bottom panels of Figure 1, respectively. This indicates that the maximum BH mass function does not much depend on our choice of the initial binary fractions and metallicities of clusters.

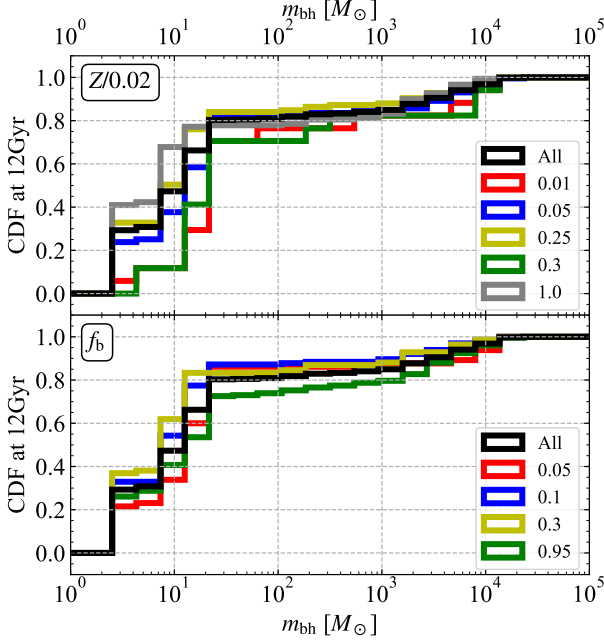
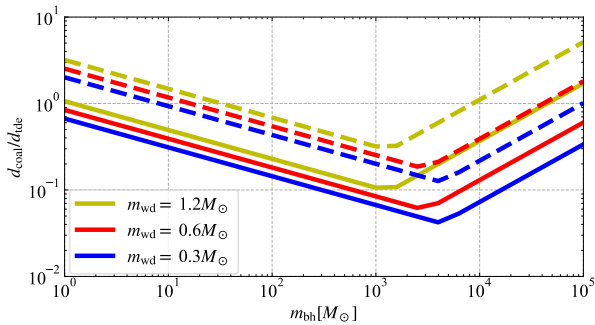
We add more about f_b . Several MOCCA models have an initial binary fraction $f_b = 0.95$, which might appear unrealistic. However, most of binary stars have wide separation, and are destroyed by perturbation of other stars throughout cluster evolution. Then, the binary fractions finally decrease to observational ones. Moreover, such high f_b can rather explain observational properties of cataclysmic variable stars (Leigh et al. 2015; Belloni et al. 2016, 2018, 2019). Thus, $f_b = 0.95$ is not too large.

In the following, we consider only unbound WD-BH coalescence events, labeling them as WD TDE candidates. We exclude from the analysis WD-BH binary coalescence, because in this type of events the binary undergoes stable mass transfer from the WD onto the BH over a timescale much longer than WD TDE typical time.

In MOCCA models, a BH coalesces with a WD when their distance

Table 1. Initial conditions and setup of MOCCA-SURVEY Database I.

$N/10^5$	R_t [pc]	R_t/R_h	W_0	$Z/0.02$	f_b	Natal kicks	N_{cl}
0.4	30, 60, 120	25, 50, Filling	3.0, 6.0, 9.0	0.05, 0.25, 1.0	0.05, 0.1, 0.3, 0.95	Fallback	243 (243)
1.0	30, 60, 120	25, 50, Filling	3.0, 6.0, 9.0	0.05, 0.25, 1.0	0.05, 0.1, 0.3, 0.95	Fallback	268 (268)
4.0	30, 60, 120	25, 50, Filling	3.0, 6.0, 9.0	0.05	0.1, 0.3, 0.95	Fallback	83 (64)
7.0	30, 60, 120	25, 50, Filling	3.0, 6.0, 9.0	0.01, 0.05, 0.25, 0.3, 1.0	0.1, 0.3, 0.95	Fallback	325 (254)
12	30, 60, 120	25, 50, Filling	3.0, 6.0, 9.0	0.05	0.05, 0.1, 0.95	Fallback	96 (71)

**Figure 1.** Cumulative distribution function (CDF) of the maximum BH mass in all the cluster models shown in Table 1. The ages of the clusters are 12 Gyr old. 476 of 1015 clusters are disrupted or fall into galactic centers before this, and are not included in the CDFs. The black curves indicate the CDFs of all the cluster models, and other curves indicate the CDFs of cluster models with different metallicity (top) and initial binary fraction (bottom).**Figure 2.** Ratio of a coalescence distance in the MOCCA models (d_{coal}) to a tidal disruption distance (d_{tde}) as a function of BH mass (m_{bh}). Solid and dashed curves indicate the collision and few-body cases (see the main text), respectively. Colors indicate WD masses (m_{wd}).

is less than the sum of their radii, if they do not have companion stars (hereafter, a collision case). Note that the BH radius is defined as its Schwarzschild radius. A BH also coalesces with a WD when their distance is less than 3 times the sum of their radii, if either of the BH and WD have companion stars (hereafter, a few-body case). Thus, the MOCCA coalescence distance (d_{coal}) can be written as

$$d_{\text{coal}} = \zeta \left(R_* + \frac{2Gm_{\text{bh}}}{c^2} \right), \quad (1)$$

and

$$\zeta = \begin{cases} 1 & (\text{collision case}) \\ 3 & (\text{few-body case}) \end{cases}. \quad (2)$$

where G is the gravitational constant, c is the light speed, m_{bh} is the BH mass, and R_* is the WD radius. However, a WD is tidally disrupted by a BH when their distance is less than a tidal disruption distance, expressed as

$$d_{\text{tde}} = \eta \left(\frac{m_{\text{bh}}}{m_*} \right)^{1/3} R_*, \quad (3)$$

where η is a numerical factor close to 1, and m_* is the WD mass. Figure 2 shows the ratio between the MOCCA coalescence distance (d_{coal}) and the tidal disruption distance (d_{tde}) as a function of the BH mass. This ratio shows a clear minimum at $m_{\text{bh}} \sim 10^3 M_{\odot}$. The ratio first decreases for $m_{\text{bh}} \lesssim 10^3 M_{\odot}$, and next increases for $m_{\text{bh}} \gtrsim 10^3 M_{\odot}$. For the smaller- m_{bh} range, d_{coal} depends on WD radii, not BH radii. Thus, $d_{\text{coal}}/d_{\text{tde}}$ decreases as d_{tde} increases with m_{bh} . For the larger- m_{bh} range, d_{coal} is proportional to m_{bh} . On the other hand, d_{tde} is proportional to the cube root of m_{bh} . Thus, $d_{\text{coal}}/d_{\text{tde}}$ increases with m_{bh} . We see that the $d_{\text{coal}}/d_{\text{tde}}$ ratio is < 1 in the whole $10^2 - 10^4 M_{\odot}$ range, thus implying that d_{coal} is a likely too stringent condition to identify WD TDE candidate and might lead to underestimate the actual WD TDE rate.

It should be noted that even the case in which d_{tde} equals d_{coal} would not imply necessarily a WD TDE. In fact, if the orbital pericenter is smaller than the BH radius, the WD undergoes a direct plunge without EM emission, whilst if the orbital pericenter is smaller than the WD radius the BH will enter the WD structure and settles in its center, forming a TZO (Thorne & Zytkov 1975), whose EM emission is expected to significantly differ from a WD TDE. We thus exclude direct plunges and TZO objects from our analysis.

Based on the aforementioned issue, we derive the number of WD TDEs in two ways. In one way, we simply count the number of WD-BH coalescence returned by MOCCA. In other words, the number of WD TDEs is the number of WD-BH coalescence. In the other way, we multiply include in the calculation a corrective factor defined as $(d_{\text{tde}}/d_{\text{coal}})F_{\text{tde}}$ (see below). Here, $(d_{\text{tde}}/d_{\text{coal}})$ serves to take into account the fact that the cross section of an interaction scales with the distance between the two objects. The F_{tde} factor, instead, excludes plunging events and TZO objects, and it is defined as:

$$F_{\text{tde}} = \max \left[1 - \frac{\max(R_*, R_{\text{sch}})}{d_{\text{tde}}}, 0 \right], \quad (4)$$

where R_{sch} is the Schwarzschild radius of the BH. The outer max of Eq. (4) indicates that a WD TDE cannot happen if either of the WD and BH radii is larger than the tidal disruption distance. The inner max of Eq. (4) decides which object plunges into which object. The two ways give the lower and upper bounds of the WD TDE rate with uncertainty from the disagreement between the tidal disruption and coalescence distances. We define the corrective factor, such that

$$C_{\text{tde}} = \begin{cases} (d_{\text{tde}}/d_{\text{coal}})F_{\text{tde}} & \text{(case I)} \\ 1 & \text{(case II)} \end{cases} \quad (5)$$

The two corrective factors are representatives of two extreme cases. The true corrective factor will be in between the two factors. In the following, we focus on the case I, whilst we discuss the outcomes of the case II in Appendix B.

Once WD-BH coalescence events are retrieved from the MOCCA database, we derive the WD TDE rate density (\mathcal{R}), i.e. the number of WD TDEs per unit time and volume. Here, we describe a method to obtain the WD TDE rate density differentiated by a set of WD TDE properties \mathcal{P} (hereafter, the differential rate density). Note that \mathcal{P} represents several quantities, such as BH mass (m_{bh}) and WD mass (m_{wd}). The method is based on Bulik et al. (2004) and Askar et al. (2017a). The differential rate density can be calculated as

$$\frac{d\mathcal{R}}{d\mathcal{P}} = \sum_{i=\text{GC, YMC}} \int_0^{T_{\text{Hubble}}} dt \frac{\text{SFR}_i(z(t))}{M_{\text{av},i}} \frac{dN_i}{dt d\mathcal{P}}. \quad (6)$$

As seen in Eq. (6), we calculate WD TDE rates in GCs and YMCs separately. We define $\text{SFR}_i(z(t))$ as the cluster formation rate density in mass at the lookback time t , and $M_{\text{av},i}$ as the average cluster mass. We represent N_i as the total number of WD TDEs in a cluster. Thus, differentiating N_i by the cluster age t , we can get dN_i/dt as the WD TDE rate at the cluster age t , and $dN_i/dt d\mathcal{P}$ as the WD TDE rate per a property at the cluster age t . Solving Eq. (6) thus returns the WD TDE rate density for a given property (e.g. BH or WD mass, see below).

We discretize Eq. (6) in such a way that the differential number of WD TDEs is given by:

$$\frac{dN_i}{dt d\mathcal{P}} = \frac{1}{N_{\text{sim},i}} \sum_{j=1}^{N_i} \delta(t - t^j) \delta(\mathcal{P} - \mathcal{P}^j) \left(\prod_k C_{\text{tde}}^{jk} \right), \quad (7)$$

where $N_{\text{sim},i}$ is the number of all the simulations, N_i is the total number of WD-BH coalescences in all the simulations, and δ functions have usual meanings. The superscript j indicates quantities of j -th WD-BH coalescence in all the simulations. The product of corrective factors considers that a WD TDE can accompany another TDEs. Note that we can get the total number of WD-BH coalescence in a cluster (N_i), if we exclude the δ functions and the product of corrective factors. Finally, we can obtain a discretized rate density in the current universe, substituting Eq. (7) into Eq. (6), such that

$$\frac{d\mathcal{R}}{d\mathcal{P}} = \sum_{i=\text{GC, YMC}} \left[\sum_j \frac{\text{SFR}_i(z(t^j))}{M_{\text{sim},i}} \delta(\mathcal{P} - \mathcal{P}^j) \left(\prod_k C_{\text{tde}}^{jk} \right) \right], \quad (8)$$

where $M_{\text{sim},i} (= M_{\text{av},i} N_{\text{sim},i})$ is the total mass of clusters in all the simulations. We give examples of use for Eq. (8). We can get the differential rate density of simple WD TDEs as

$$\begin{aligned} \frac{d\mathcal{R}}{dm_{\text{bh}} dm_{\text{wd}}} &= \sum_{i=\text{GC, YMC}} \left[\sum_j \frac{\text{SFR}_i(z(t^j))}{M_{\text{sim},i}} \delta(m_{\text{bh}} - m_{\text{bh}}^j) \delta(m_{\text{wd}} - m_{\text{wd}}^j) C_{\text{tde}}^j \right]. \end{aligned} \quad (9)$$

Table 2. Properties of GCs and YMCs in the database

Clusters	$N_{\text{sim},i}$	$M_{\text{sim},i} [M_{\odot}]$	$M_{\text{av}} [M_{\odot}]$
GC	1015	$3.0 \times 10^8 M_{\odot}$	$2.8 \times 10^5 M_{\odot}$
YMC	174	$8.8 \times 10^6 M_{\odot}$	$5.1 \times 10^4 M_{\odot}$

On the other hand, we can express the differential rate density of WD TDEs with another TDE as

$$\begin{aligned} \frac{d\mathcal{R}}{dm_{\text{bh}} dm_{\text{wd}} dm_*} &= \sum_{i=\text{GC, YMC}} \left[\sum_j \frac{\text{SFR}_i(z(t^j))}{M_{\text{sim},i}} \delta(m_{\text{bh}} - m_{\text{bh}}^j) \right. \\ &\quad \left. \times \delta(m_{\text{wd}} - m_{\text{wd}}^j) \delta(m_* - m_*^j) C_{\text{tde}}^{\text{wd}} C_{\text{tde}}^* \right], \end{aligned} \quad (10)$$

where m_* is the mass of another star disrupted simultaneously with the WD.

We also define a volume-limited WD TDE rate as

$$\mathcal{S} = \int_0^{z_{\text{max}}} \mathcal{R}(z) \frac{dV(z)}{dz} dz, \quad (11)$$

where $\mathcal{R}(z)$ and $V(z)$ are the WD TDE rate density and comoving volume at a redshift of z , respectively. Note that we can derive $\mathcal{R}(z)$ or $d\mathcal{R}(z)/d\mathcal{P}$ when we replace T_{Hubble} with $T_{\text{Hubble}} - t_{\text{lb}}(z)$ in Eq. (6), where $t_{\text{lb}}(z)$ is a lookback time at a redshift of z . For confirmation, the unit of \mathcal{S} is the number of WD TDEs per unit time.

We adopt the GC formation rate, SFR_{GC} , estimated by Katz & Ricotti (2013), and simplify their GC formation rate as

$$\text{SFR}_{\text{GC}}(z) = \begin{cases} 0.003 M_{\odot} \text{ yr}^{-1} \text{ Mpc}^{-3} & (2 \leq z \leq 8) \\ 0 & \text{(otherwise)} \end{cases}. \quad (12)$$

We set the YMC formation rate, SFR_{YMC} , as

$$\text{SFR}_{\text{YMC}}(z) = 0.016 f_{\text{YMC}} \psi(z) M_{\odot} \text{ yr}^{-1} \text{ Mpc}^{-3}, \quad (13)$$

where

$$\psi(z) = \frac{(1+z)^{2.6}}{1 + [(1+z)/3.2]^{6.2}}. \quad (14)$$

We assume the current star formation rate as $0.016 M_{\odot} \text{ yr}^{-1} \text{ Mpc}^{-3}$ (e.g. Behroozi et al. 2013), and set the fraction of YMCs to $f_{\text{YMC}} = 0.03$. The redshift dependence is the same as the star formation rate derived by Madau & Fragos (2017). We estimate the fraction of YMCs by restricting ourselves to those with an age < 1 Gyr, under the assumption that older ones will have evaporated (Krumholz et al. 2019). We ignore WD TDEs at a cluster age of more than 1 Gyr when calculating the WD TDE rate density in YMCs.

For N_{GC} , we adopt clusters surviving from dynamical friction. For N_{YMC} , we use clusters with $N \leq 10^5$ and $Z = 0.02$ as described above. We also show $N_{\text{sim},i}$, $M_{\text{sim},i}$, and $M_{\text{av},i}$ of GCs and YMCs in Table 2. We obtain the local number density of GCs as 29.1 Mpc^{-3} , combining SFR_{GC} with $M_{\text{av,GC}}$, if all the GCs survive. In fact, ~ 53 % of cluster models selected for GCs survive until 12 Gyr old. This means that the current GC number density (n_{GC}) is 15.4 Mpc^{-3} . Our value of n_{GC} is considerably larger than the estimate provided by Portegies Zwart & McMillan (2000) and Maguire et al. (2020) or the simple estimate that can be inferred from MW GCs (e.g. Rodriguez et al. 2016). Since n_{GC} represents a scale factor in our calculations, we explicitly leave this dependence in all our calculations, adopting a fiducial value of $n_{\text{GC}} = 15.4 \text{ Mpc}^{-3}$. Similarly, we infer that the number density of YMCs is 9.45 Mpc^{-3} .

Finally, we summarize three models (hereafter called models A,

Table 3. Models to calculate WD TDE rate densities

Name	IMBH formation	Eq. (5)
Model A	optimistic case	case I
Model B	optimistic case	case II
Model C	pessimistic case	case I

B, and C) to calculate the WD TDE rate density (see also Table 3). In model A, we consider the optimistic case for the IMBH formation ($f_{\text{BH,GC}} = 0.19$ as seen in Figure 1), and adopt the case I for the corrective factor C_{tde} in Eq. (5). We focus on this results in section 3. In model B, we consider the optimistic case, the same as model A, however adopt the case II for the corrective factor C_{tde} in Eq. (5). We describe the results of model B in Appendix B. In model C, we consider the pessimistic case for the IMBH formation, and adopt the case I for the corrective factor C_{tde} in Eq. (5). This results are written in Appendix C.

3 RESULTS

We obtain the total rate density of WD TDEs (\mathcal{R}) as $4.9 \times 10^2 \text{yr}^{-1} \text{Gpc}^{-3}$ in model A, and $1.1 \times 10^2 \text{yr}^{-1} \text{Gpc}^{-3}$ in model B (see Appendix B). The former is 5 times as large as the latter. This is because WD TDEs are dominated by WD TDEs of single CO and ONe WDs and single BHs with $m_{\text{bh}} \sim 10^3 - 10^4 M_{\odot}$ as shown later, and their $d_{\text{coal}}/d_{\text{tde}}$ is ~ 0.2 as seen in Figure 2. The rate density is $8.9 \times 10^1 \text{yr}^{-1} \text{Gpc}^{-3}$ in model C (see Appendix C), which is also about 5 times less than the rate density for model A. Hereafter, we focus on the rate densities and their derivatives obtained in model A. We should bear in mind that they can be overestimated by at most 5 times.

Figure 3 shows the WD TDE rate density and its breakdowns. As seen in the top left panel, a majority of WD TDEs happen in BHs with $m_{\text{bh}} \gtrsim 10^3 M_{\odot}$. The fraction of WD TDEs with $m_{\text{bh}} \lesssim 10^3 M_{\odot}$ is less than 10 %. This is not because there are more many clusters with $\gtrsim 10^3 M_{\odot}$ BHs than with $\lesssim 10^3 M_{\odot}$ BHs, but because more massive BHs yield WD TDEs much more frequently. This will be seen in Eq. (19) of section 4. The WD TDE rate decreases for $m_{\text{bh}} \gtrsim 10^4 M_{\odot}$ in two steps. First, WDs tend to be just swallowed by BHs without tidally disrupted. Second, clusters cannot form BHs with more than several $10^4 M_{\odot}$.

As seen on the top right corner, more than 90 % of WD TDEs happen in GCs, and the rest in YMCs. This is not only because the local number density of GCs is larger than that of YMCs, but also because GCs harbor much more massive BHs than YMCs. GCs can have $\gtrsim 10^4 M_{\odot}$ BHs, while YMCs can have $\lesssim 10^4 M_{\odot}$ BHs (see the top left panel of Figure 3). Since we assume that YMCs have smaller masses and shorter lifetimes than GCs, YMCs cannot yield $\gtrsim 10^4 M_{\odot}$ BHs. Interestingly, YMCs dominate WD TDEs with $\lesssim 10^2 M_{\odot}$ BHs, although such WD TDEs are minor on the whole of WD TDEs.

We can see the WD mass distribution from the bottom right panel of Figure 3. The WD TDE rate suddenly increases above $m_{\text{wd}} \sim 0.5 M_{\odot}$. $\gtrsim 0.5 M_{\odot}$ WDs (CO and ONe WDs) can be formed through single star evolution within the Hubble time. On the other hand, $\lesssim 0.5 M_{\odot}$ WDs (He WDs) cannot be formed through single star evolution within the Hubble time, and can be formed only through binary star evolution. For $m_{\text{wd}} \gtrsim 0.5 M_{\odot}$, the WD TDE rate gradually decreases with m_{wd} increasing for the following two reasons. First, the Kroupa's IMF yields a smaller number of more massive WDs.

Second, more massive WDs can be more easily swallowed by BHs without tidally disrupted. This can be clearly seen for $m_{\text{wd}} \gtrsim 1.2 M_{\odot}$.

The abundance of He WD, CO WD, and ONe WD TDEs is ~ 2.2 , 88, and 10 % of the total WD TDEs, respectively. In order to compare this abundance with the abundance of WDs yielded through single star evolution, we prepare $Z = 0.02$ single stars with the Kroupa's IMF, and calculate their 15 Gyr evolutions by the SSE code (Hurley et al. 2000). Then, the abundance of He, CO, and ONe WDs is 0, 97.5, and 2.5 %, respectively. The former WD abundance is quite different from the latter WD abundance. Single star evolution cannot form He WDs for 15 Gyr, while binary star evolution forms He WDs, and yields He WD TDEs. The abundance of ONe WD TDEs is ~ 4 times larger than the abundance of ONe WDs from single stars. Moreover, the abundance of $\sim 1 M_{\odot}$ CO WD TDEs is ~ 10 times larger than the abundance of CO WDs from single stars, compared between the solid and dashed red curves in the bottom right panel of Figure 3. WD TDEs prefer to more massive WDs, except that binary star evolution yield He WD TDEs.

The reason why WD TDEs prefer to more massive WDs is mass segregation by which more massive objects fall into the GC center more preferentially. Figure 4 shows the number of stars in a GC and in its inner region as a function of stellar masses. The number ratio of ONe WDs with $\sim 1.4 M_{\odot}$ to CO WDs with $\sim 0.5 M_{\odot}$ is 1/30 for the whole GC, and 1/3 for its inner region. Thus, more massive WDs experience WD TDEs more easily.

He WDs also sink into the inner region preferentially despite of their small masses. The ratio of He WDs with $\sim 0.4 M_{\odot}$ to CO WDs with $\sim 0.5 M_{\odot}$ is 1/100 for the whole GC, and 1/30 for the inner region. This is because He WDs are likely to be binary members owing to their formation mechanism. The total masses of these He WDs and their companions are larger than the surrounding stars, and these He WDs sink into the inner region with their companions. This may be the reason why He WD TDEs still happen frequently despite of the small masses of He WDs.

$0-0.05 M_{\odot}$ CO WDs and He WDs equally contribute to the WD TDE rate. Thus, the red curve overlaps on the blue curve in the smallest histogram bin in the lower right panel of Figure 3. Such low-mass CO WDs are formed as follows. A binary star evolves to a close binary star with two CO WDs. The separation of the close binary star shrinks due to gravitational wave radiation, and the lighter CO WD fills its Roche lobe at some point. When the mass ratio of the lighter CO WD to the heavier CO WD is smaller than ~ 0.6 , the mass transfer from the lighter CO WD to the heavier CO WD is stable. Thus, the lighter CO WD gradually loses its mass down to $\lesssim 0.05 M_{\odot}$ without the merger of the two CO WDs. The tidally disrupted CO WDs have a mass gap between 0.05 and $0.3 M_{\odot}$. This is because the mass-loss timescale from $\sim 0.3 M_{\odot}$ to $\sim 0.05 M_{\odot}$ is much shorter than that from $\sim 0.05 M_{\odot}$ to $\sim 0 M_{\odot}$.

The top left panel of Figure 3 also shows the rate density of multiple TDEs (defined in the caption of Figure 3). In multiple TDEs, a series of TDEs should happen at time intervals of an order of the maximum periods of binaries involving these encounters¹. We find that 80 % of these binaries have periods of less than 100 days. Thus, multiple TDEs can be observed as single (but resolvable) transient events at the same time and location.

Multiple TDEs are most likely to occur with $\sim 10^3 M_{\odot}$ BHs, despite that the WD TDE rate increase with m_{bh} increasing (see the

¹ This is just a rough estimate. If multiple TDEs occur in temporary (but long-lived) multiple stellar systems (so-called resonant encounters), the intervals of TDEs can be much more than the maximum periods of binaries.

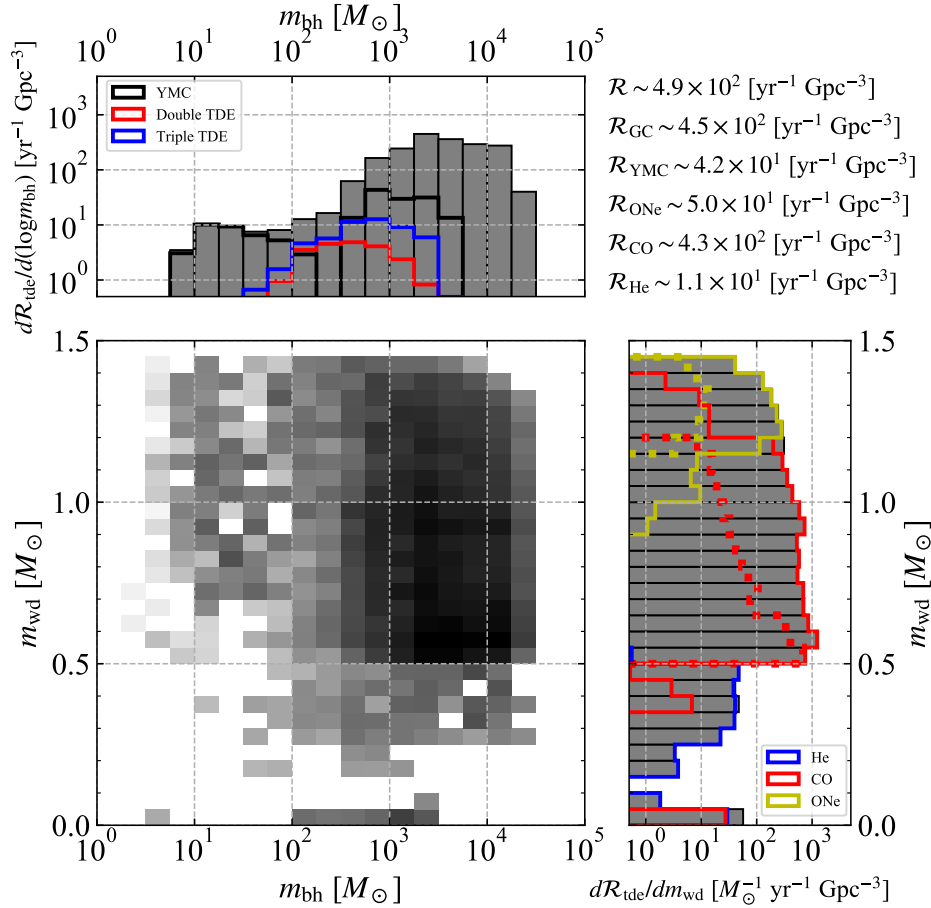


Figure 3. WD TDE rate density in the current GCs and YMCs. On the top-right corner, we show the rate densities of all WD TDEs (\mathcal{R}), WD TDEs in GCs (\mathcal{R}_{GC}), WD TDEs in YMCs (\mathcal{R}_{YMC}), ONe WD TDEs (\mathcal{R}_{ONe}), CO WD TDEs (\mathcal{R}_{CO}), and He WD TDEs (\mathcal{R}_{He}). We call double and triple TDEs “multiple TDEs” all together. A multiple TDE is defined as a phenomenon where a WD TDE happens along with another TDEs in a binary-single or binary-binary encounter. Another TDEs do not have to be WD TDEs. Multiple TDEs can contain two or three WD TDEs. We count them as twice, and three times WD TDEs. Bottom left: Relative abundance of the rate density per m_{wd} per dex of m_{bh} in a logarithmic color scale. Top left: The rate density per dex of m_{bh} . Gray-filled histograms indicate all the WD TDEs, and black-open histograms WD TDEs only in YMCs. Red- and blue-open histograms show WD TDEs in double and triple TDEs, respectively. Bottom right: The rate density per m_{wd} . Gray-filled histograms are the same as in the top left panel. Yellow-, red-, and blue-open histograms indicate ONe WD, CO WD, and He WD TDEs, respectively. Yellow- and red-dotted curves show the abundance of ONe WDs and CO WDs, respectively, yielded through single star evolution. We obtain this abundance as follows. We prepare $Z = 0.02$ single stars with the Kroupa’s IMF, and calculate their 15 Gyr evolutions by the SSE code (Hurley et al. 2000). The abundance of $0.5 - 0.55 M_{\odot}$ CO WDs is normalized to the rate density per m_{bh} at $0.5 - 0.55 M_{\odot}$. He WDs are not formed within 15 Gyr through single star evolution.

top left panel of Figure 3). This can be interpreted as follows. Figure 5 shows that the binary fractions in the inner regions of GCs become smaller with m_{bh} increasing. Since multiple TDEs need binary stars, they are harder to happen in GCs with larger m_{bh} . In the process of BH growth, the BHs disrupt binary stars by unbinding them, or by swallowing either of them.

Figure 6 shows the double TDE rate density. The total rate density is $\sim 4.1 \text{ yr}^{-1} \text{ Gpc}^{-3}$, i.e. only $\sim 0.84 \%$ of the total WD TDEs. The double TDEs in YMCs are only 4.3% of the total double TDEs. Most of the double TDEs consist of WDs and main sequences (MSs), or of WDs and post MSs (PMSs). The reason for the abundant MSs is that MSs have long lifetimes, and relatively large radii $\sim 1 R_{\odot}$. The reason for the abundance PMSs is that PMSs have large radii $\gg 1 R_{\odot}$, although their lifetimes are not long.

The rate density weakly depends on WD masses for $m_{\text{wd}} \geq 0.5 M_{\odot}$, or for CO and ONe WDs. Mass segregation strongly af-

fects the WD mass function of double TDEs. The rate density with He WDs is similar to those with CO and ONe WDs. This is because most of He WDs have their companions due to their formation processes. The companion mass distribution has a peak at $0.7 - 1.0 M_{\odot}$, which consists of MSs and PMSs. The mass of $\sim 1.0 M_{\odot}$ corresponds to the turn-off mass at ~ 12 Gyr. The number of $> 1.0 M_{\odot}$ MS and PMS stars is small, since these stars already evolve to stellar remnants. Nevertheless, double TDEs can contain $> 1.0 M_{\odot}$ MSs and PMSs. These stars experience stellar coalescence or mass transfer from their companions before they are tidally disrupted.

Figure 7 shows the triple TDE rate density. The total rate density is $\sim 8.2 \text{ yr}^{-1} \text{ Gpc}^{-3}$, similar to the double TDE rate density, and only $\sim 1.7 \%$ of the total WD TDE rate density. The major part is dominated by WD TDEs with MS and PMS TDEs. Interestingly, a WD TDE can accompany another WD TDE in triple TDEs. 17% of

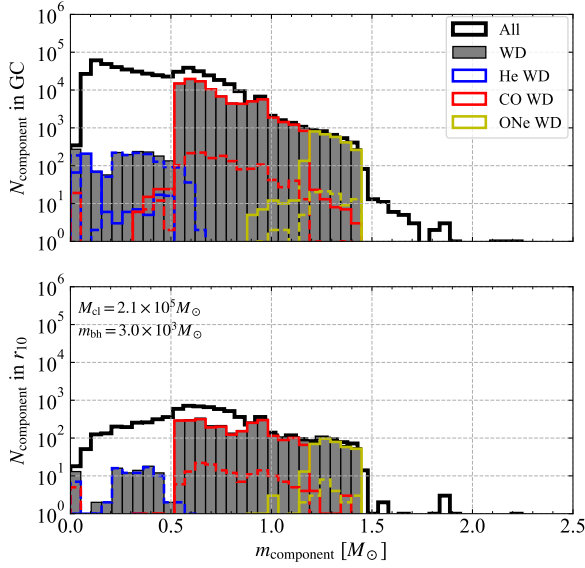


Figure 4. Number of stars in a cluster (top) and in its 10 % Lagrangian radius (bottom) as a function of stellar masses. The age of the cluster is 12 Gyr, and the cluster has $N = 7 \times 10^5$, $R_t = 30$ pc, $R_t/R_h = 50$, $W_0 = 6$, and $Z = 0.001$ at the initial time. We exclude the most massive BH to obtain the 10 % Lagrangian radius. We count a binary star as two stars. Solid black curves indicate all the stars. Filled histograms show all the WDs. Solid blue, red, and yellow curves indicate He, CO, and ONe WDs. Dashed blue, red, and yellow curves indicate He, CO, and ONe WDs in binaries.

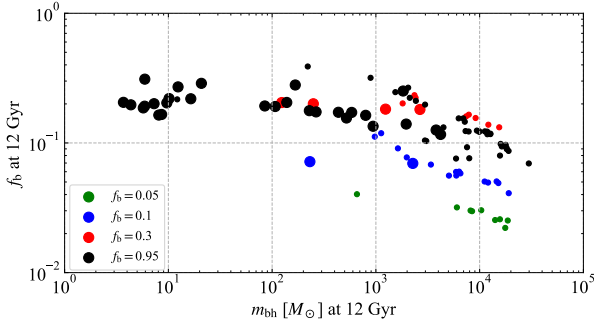


Figure 5. Binary fraction in the 10 % Lagrangian radius of each GC at 12 Gyr as a function of the most massive BH mass. We exclude the most massive BH to obtain the 10 % Lagrangian radius. We do not plot a GC if it has a BH whose mass is half of the GC mass. Color coding indicates the binary fraction of each GC at the initial time. Large dots indicate GCs with multiple TDEs including at least one WD TDE, and small dots indicate GCs with WD TDEs but without multiple TDEs.

triple TDEs (or 0.35 % of the total WD TDEs) can include double WD TDEs.

The WD mass distribution in the triple TDE rate density is similar to that in the double TDE rate density (see the bottom right panel of Figure 6). The mass distributions of non-WD stars in triple TDEs are also similar to that in double TDEs. There are peaks at $\sim 1.0 M_\odot$. The mass of $\sim 1.0 M_\odot$ corresponds to the turn-off mass at ~ 12 Gyr.

Figure 8 shows the WD TDE rate within a redshift of 0.3

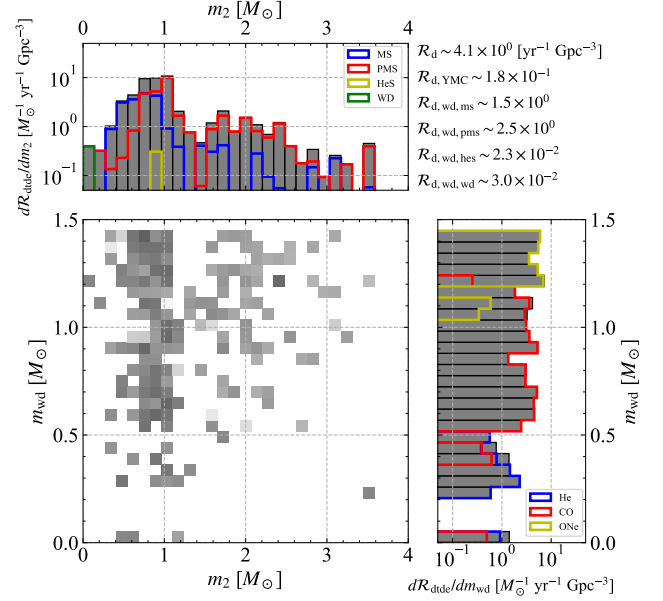


Figure 6. Double TDE rate density in the current GCs and YMCs. On the top-right corner, we show the rate densities of all double TDEs (\mathcal{R}_d), those in YMCs ($\mathcal{R}_{d, \text{YMC}}$), those with WD and main sequence (MS) ($\mathcal{R}_{d, \text{wd, ms}}$), those with WD and post MS (PMS) ($\mathcal{R}_{d, \text{wd, pms}}$), those with WD and helium stars (HeS) ($\mathcal{R}_{d, \text{wd, hes}}$), and those with two WDs ($\mathcal{R}_{d, \text{wd, wd}}$). Bottom left: Relative abundance of the rate density per m_{wd} per companion mass (m_2). Top left: The rate density per m_2 . Gray-filled histograms indicate all the double TDEs. Colored-open histograms indicate stellar types of companion stars, such that blue-, red-, yellow-, and green-open histograms are MSs, PMSs, HeSs, and WDs, respectively. Bottom right: The rate density per m_{wd} . Gray-filled histograms indicate all the double TDEs. Colored-open histograms indicate WD types, such that blue-, red-, and yellow-open histograms are He, CO, and ONe WDs, respectively.

(the volume-limited WD TDE rate), obtained from Eq. (11) for $z_{\text{max}} = 0.3$. The reason for making this figure is that WD TDEs can be observed in the low-redshift universe. We find small differences between the WD TDE rate density and volume-limited WD TDE rate. The contribution of GCs in the volume-limited WD TDE rate is smaller than in the WD TDE rate density. YMCs are more actively formed in a higher-redshift universe. Moreover, IMBHs in GCs do not yet end their growth in the redshift of 0.3. The relative abundance of CO WDs with $\sim 0.5 M_\odot$ decreases from the WD TDE rate density to the volume-limited WD TDE rate. Such CO WDs are not yet formed, because the lifetimes of their progenitors are longer than the universe age at the redshift of 0.3. Thus, more massive WDs become more dominant in the volume-limited WD TDE rate.

4 COMPARISON WITH PREVIOUS STUDIES

In section 3, we see that the total WD TDE rate density in GCs is $\sim 4.5 \times 10^2 \text{ yr}^{-1} \text{ Gpc}^{-3}$. On the other hand, Maguire et al. (2020) have estimated that the total rate density is $\sim 4 f_{\text{BH, GC}} \text{ yr}^{-1} \text{ Gpc}^{-3} \sim 0.8 \text{ yr}^{-1} \text{ Gpc}^{-3}$, if GCs in dwarf galaxies are included. Here, we adopt $f_{\text{BH, GC}} = 0.19$ for the fraction of GCs with IMBHs to the total GCs in the local universe as described in section 2. Our current GC number density is 15.4 Mpc^{-3} . Maguire et al. (2020) have supposed that the current GC number density is 5.35 Mpc^{-3} . Although our current GC

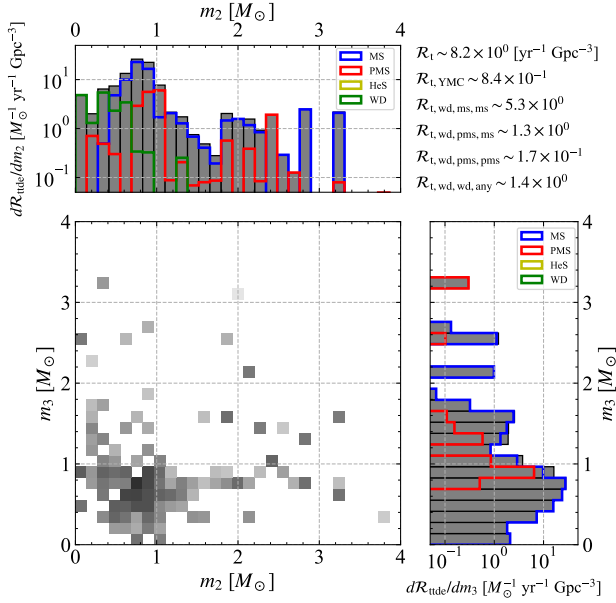


Figure 7. Triple TDE rate density in the current GCs and YMCs. We sort three disrupted stars in the order of ONe WD, CO WD, He WD, HeS, PMS, and MS, and in the descending order of masses if the stellar types are the same. We denote the first and second companion masses as m_2 and m_3 , respectively. On the top-right corner, we show the rate densities of all triple TDEs (\mathcal{R}_t), those in YMCs ($\mathcal{R}_{t, \text{YMC}}$), those with WD and two MSs ($\mathcal{R}_{t, \text{wd, ms, ms}}$), those with WD, MS, and PMS ($\mathcal{R}_{t, \text{wd, ms, pms}}$), those with WD and two PMSs ($\mathcal{R}_{t, \text{wd, pms, pms}}$), and those with two WDs and any type star ($\mathcal{R}_{t, \text{wd, wd, any}}$). Bottom left: Relative abundance of the rate density per m_2 and per m_3 . Top left: The rate density per m_2 . Gray-filled histograms indicate all the triple TDEs. Colored-open histograms indicate stellar types of companion stars, such that blue-, red-, yellow-, and green-open histograms are MSs, PMSs, HeSs, and WDs, respectively. Bottom right: The rate density per m_3 . Color codes are the same as the top left panel.

number density is 3 times larger than theirs, the difference between assumed GC number densities cannot explain the difference between the derived rate densities. This means that we get a WD TDE rate in each GC ~ 100 larger than adopted by Maguire et al. (2020). They have adopted a WD TDE rate in each GC calculated by Baumgardt et al. (2004a). In this section, we will make clear the reason why our WD TDE rate in each GC is much larger than obtained by Baumgardt et al. (2004a).

We can understand a WD TDE rate in each cluster, using the loss cone theory developed by Frank & Rees (1976). Moreover, we can also interpret the difference between previous and our results in the framework of the loss cone theory. Here, we first introduce the loss cone theory briefly.

In the loss cone theory, a TDE occurs when a star keeps a loss-cone orbit on its orbital time without diffused by two-body relaxation. Based on the theory, Baumgardt et al. (2004a) (see also Baumgardt et al. 2004b) have derived their eq. (7), the description of a TDE rate in a cluster (D), as

$$D = k_D G^{1/2} \left[\frac{R_*^{9-4\alpha} v_0^{7(16/3)\alpha-5}}{m_{\text{bh}}^{(19/3)\alpha-9}} \right]^{1/(8-2\alpha)}, \quad (15)$$

where k_D is a dimensionless coefficient. We assume that a cluster harbors an IMBH, and that the IMBH is surrounded by a stellar cusp

in which the stellar number density is written as $n = v_0 r^{-\alpha}$, where n is the stellar number density, and r is the distance from the IMBH. If the IMBH mass is sufficiently smaller than a cluster mass, the stellar cusp is contained in a constant density core with density n_c at the influence radius of the IMBH r_{infl} . The influence radius can be written as

$$r_{\text{infl}} = \frac{G m_{\text{bh}}}{\gamma v_c^2} \quad (16)$$

where v_c is the velocity dispersion in the core, and γ is a numerical factor. Finally, we can rewrite Eq. (15) as

$$D = k_D G^{1/2+\alpha\beta} \gamma^{-\alpha\beta} R_*^{2-\beta} m_*^{(-8/3)+(7/3)\beta} m_{\text{bh}}^{(19/6)+(\alpha-7/3)\beta} n_c^\beta v_c^{-2\alpha\beta}, \quad (17)$$

where $\beta = 7/[2(4-\alpha)]$.

We can adopt $\alpha = 7/4$ for WDs in our clusters. This is consistent with our 3D profile in Figure 9, and with the results of Baumgardt et al. (2004a). This means that WDs form so-called Bahcall-Wolf cusp (Bahcall & Wolf 1976). This is because WD masses range from the minimum stellar mass ($\sim 0.1 M_\odot$) to the maximum stellar mass ($\sim 1.4 M_\odot$) except for minor objects growing through stellar mergers. Note that a stellar cusp made of MSs can have $\alpha \sim 3/2$ as seen in Baumgardt et al. (2004a), since the maximum MS mass is at most $\sim 1.0 M_\odot$.

For $\alpha = 7/4$, we can rewrite Eq. (17) as

$$D = \gamma^{-49/18} k_D G^{29/9} R_*^{4/9} m_*^{26/27} m_{\text{bh}}^{61/27} n_c^{14/9} v_c^{-49/9} \quad (18)$$

$$\sim 10^4 \text{ Gyr}^{-1} \left(\frac{k_D}{30} \right) \left(\frac{\gamma}{0.3} \right)^{-49/18} \left(\frac{R_*}{1 R_\odot} \right)^{4/9} \left(\frac{m}{1 M_\odot} \right)^{26/27} \times \left(\frac{m_{\text{bh}}}{10^3 M_\odot} \right)^{61/27} \left(\frac{n_c}{10^5 \text{ pc}^{-3}} \right)^{14/9} \left(\frac{v_c}{10 \text{ km s}^{-1}} \right)^{-49/9}. \quad (19)$$

We adopt $R_* = 1 R_\odot$, $m = 1 M_\odot$, $m_{\text{bh}} = 10^3 M_\odot$, $n_c = 10^5 \text{ pc}^{-3}$, and $v_c = 10 \text{ km s}^{-1}$ for comparison with Baumgardt et al. (2004a), despite that WD radii are typically $\ll 1 R_\odot$. We choose $k_D = 30$, which is consistent with the choice of $k_D = 65$ in Baumgardt et al. (2004a). We set $\gamma = 0.3$ based on stellar number density profiles. On the other hand, Baumgardt et al. (2004a) have set $\gamma = 2$. As seen in Figure 9, γ is better for the choice. The velocity dispersion starts increasing inside of the influence radius with $\gamma = 0.3$ (see the bottom panel). The influence radius with $\gamma = 2$ is completely inside of the stellar cusp. For confirmation, we choose $\gamma = 0.3$ (the vertical gray lines in Figure 9), not $\gamma = 2$ (the vertical black lines in Figure 9). We just refer to $\gamma = 2$ to compare our results with previous studies. We will later show that γ critically affects the difference between the results of Baumgardt et al. (2004a) and ours.

We compare Eq. (19) with our simulation results. We define a scaled TDE rate \hat{D} as

$$\hat{D} = D \left(\frac{R_*}{1 R_\odot} \right)^{-4/9} \left(\frac{m}{1 M_\odot} \right)^{-26/27} \left(\frac{n_c}{10^5 \text{ pc}^{-3}} \right)^{-14/9} \left(\frac{v_c}{10 \text{ km s}^{-1}} \right)^{49/9}. \quad (20)$$

We calculate \hat{D} as follows. We calculate a rate of WD-BH coalescence in each cluster during its age of 10 – 13 Gyr. We convert the rate into a WD TDE rate (D), using the corrective factor described in the case I of Eq. (5). We pick up cluster profiles at their ages of 12 Gyr, and obtain n_c and v_c as the stellar number density and velocity dispersion, respectively, at a radius whose enclosed mass is the same as the maximum BH mass aside from the BH itself. This assumption is valid only when the stellar phase space distribution is isothermal, or only when the radius is inside the stellar core. In fact, the radius is always inside the stellar core for $m_{\text{bh}} \lesssim 10^4 M_\odot$.

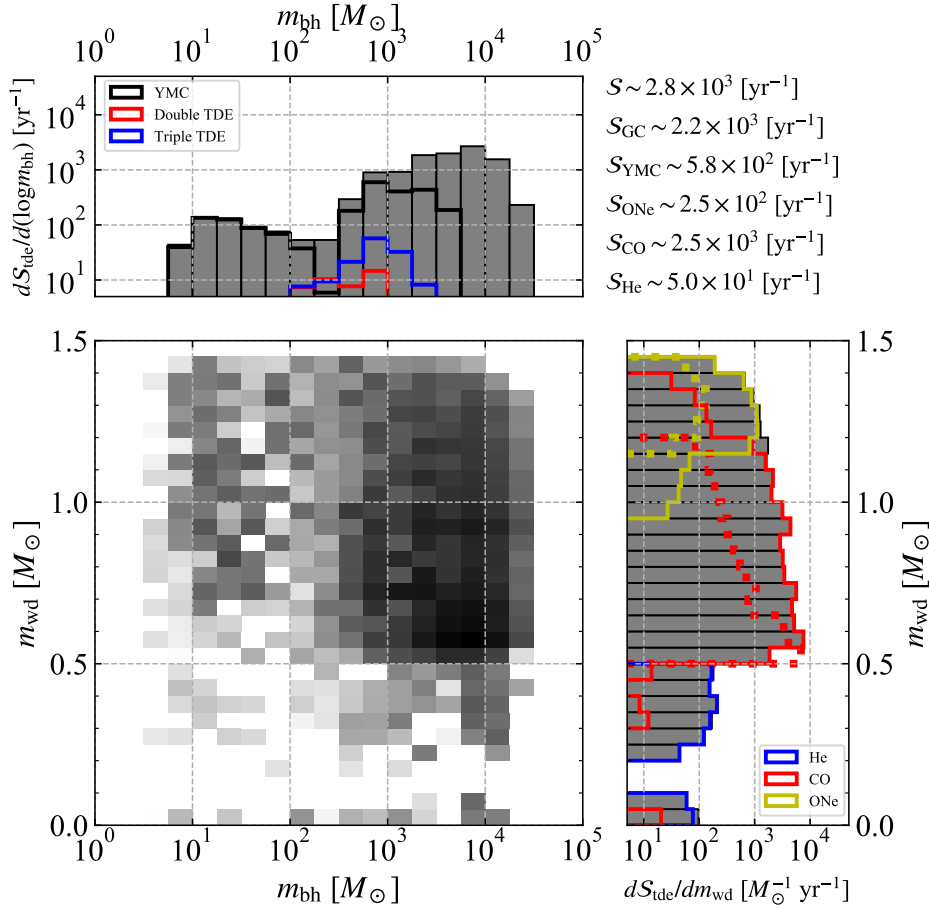


Figure 8. The same as Figure 3 except that the WD TDE rate density in the local universe is replaced with the WD TDE rate within a redshift of 0.3 (the volume-limited WD TDE rate).

We plot \hat{D} in Eq. (20) and \hat{D} of each cluster in Figure 10, where we exclude clusters with $m_{\text{bh}}/M_{\text{cl}} > 0.5$, since we cannot define n_{c} and v_{c} for them. We cannot plot clusters with $\hat{D} = 0$ due to the logarithmic scale. Instead, the presence of such clusters is indicated by arrows with bars. We find many clusters with $\hat{D} = 0$ for $m_{\text{bh}} = 1 - 50 M_{\odot}$. On the other hand, there are only 3 clusters with $\hat{D} = 0$ for $m_{\text{bh}} = 50 - 300 M_{\odot}$. There are no clusters with $\hat{D} = 0$ for $m_{\text{bh}} > 300 M_{\odot}$.

We can see that \hat{D} in Eq. (20) agrees with \hat{D} of clusters for $10^2 M_{\odot} \lesssim m_{\text{bh}} \lesssim 10^4 M_{\odot}$. This means that WD TDE rates follow the loss cone theory for this BH mass range. We expect that this is true for clusters with $m_{\text{bh}}/M_{\text{cl}} > 0.5$. The WD TDE rates should deviate from the theory when $m_{\text{bh}} \lesssim 10^2 M_{\odot}$. Small BHs can wander in the core, since they are easily perturbed by other stars. The theory cannot apply for this case. In fact, there are many clusters with $\hat{D} = 0$ as indicated by arrows with bars in Figure 10. It is a coincidence that \hat{D} in Eq. (20) agrees with \hat{D} of clusters with non-zero \hat{D} for $m_{\text{bh}} \lesssim 10^2 M_{\odot}$. However, this mass range has minor effects on the total WD TDE rate density, since WD TDEs do not occur much for $m_{\text{bh}} \lesssim 10^2 M_{\odot}$. For $m_{\text{bh}} \gtrsim 10^4 M_{\odot}$, the scaled WD TDE rate appears to be saturated. This is because the stellar cusps cover the stellar cores in these clusters, and directly connect with the stellar halos, not the stellar cores. Such saturation is also predicted by Stone et al. (2017). Eq. (20) is also not true for this case. Even for $m_{\text{bh}} \gtrsim 10^4 M_{\odot}$, several clusters, in particular those with smaller f_{b} , match better with \hat{D} in

Eq. (20). However, it would be a coincidence. These clusters have high BH mass fractions, $m_{\text{bh}}/M_{\text{cl}} \sim 0.4$. For such clusters, the whole clusters are stellar cusps around the BHs. Eq. (20) is not true for such clusters.

Eq. (19) may seem strange, because a $10^3 M_{\odot}$ BH should be able to grow to a $10^5 M_{\odot}$ BH if it keeps accreting $1 M_{\odot}$ stars during 10 Gyr. On the other hand, BHs in our cluster models have at most $\sim 10^4 M_{\odot}$. This discrepancy may come from the fact that BHs in our cluster models grow in the case II in Eq. (5), and Eq. (19) is deduced from the case I in Eq. (5) (i.e. model A). Actually, MS TDE rates calculated in the case I are larger than those calculated in the case II by an order of magnitude (see Figure A1 in Appendix A). Thus, we may underestimate BH masses in our cluster models by an order of magnitude at most. However, the underestimate may not be so serious for the following two reasons. First, BHs stop growing at $\sim 10^4 M_{\odot}$ due to depletion of surrounding stars as described above. Second, we assume no mass loss in TDEs in our cluster models. It should be stressed that the final fate of TDE debris is not fully understood. On the one hand, some works indicate that up to half-mass of the disrupted star could be lost in a TDE, and a considerable fraction of such mass can be ejected from the BHs (Metzger & Stone 2016; Lu & Bonnerot 2020). On the other hand, some recent simulations suggest that the fraction of ejected mass can be rather limited (Guillochon et al. 2014; Shiokawa et al. 2015).

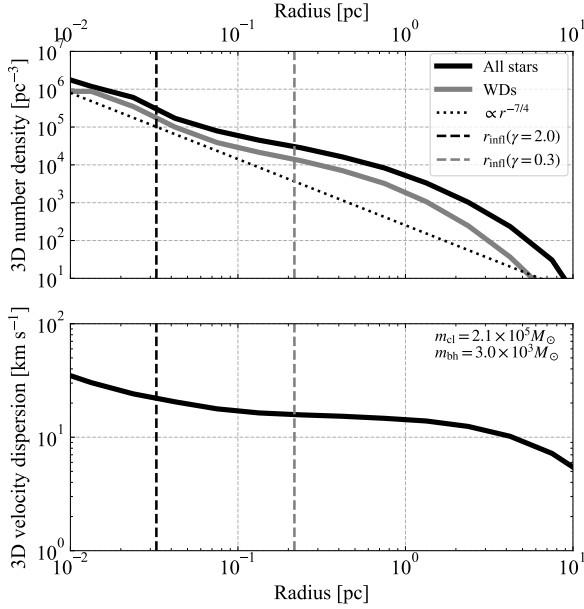


Figure 9. Profiles of 3D stellar number density (top) and 3D velocity dispersion (bottom). The age and initial conditions of the cluster is the same as in Figure 4. The current cluster mass and maximum BH mass are indicated in the bottom panel. Black- and gray-solid lines indicate profiles of all stars and WDs, respectively. The dotted line shows a stellar number density proportional to $r^{-7/4}$. The vertical black- and gray-dashed lines draw r_{infl} for $\gamma = 2$ and 0.3 , respectively, where $v_c = 15 \text{ km s}^{-1}$.

Although BH masses may be underestimated in our cluster models, Eq. (19) would be correct under the simulations where such BHs are present in clusters. WD TDE rates match well with Eq. (19) as seen in Figure 10. Moreover, MS TDE rates are also in good agreement with Eq. (19) as seen in the left panel of Figure A2 in Appendix A.

Interestingly, the scaled TDE rates do not much depend on the initial binary fractions f_b for $m_{\text{bh}} = 10^2 - 10^4 M_\odot$. This means that the initial binary fractions do not affect TDE rates if clusters have $10^2 - 10^4 M_\odot$ BHs. On the other hand, all the clusters with $\hat{D} > 0$ have $f_b = 0.95$ for $m_{\text{bh}} \lesssim 10 M_\odot$. These clusters are more massive and more dense than other clusters for $m_{\text{bh}} \lesssim 10 M_\odot$. Thus, they can have WD TDEs. The reason why such high-mass and high-density clusters do not give rise to $m_{\text{bh}} \gtrsim 10^2 M_\odot$ during 12 Gyr is that they have high binary fractions ($f_b = 0.95$), and the binary interactions prevent rapid stellar or BH mergers. Such clusters with low binary fractions ($f_b \leq 0.3$) already yield BHs with $m_{\text{bh}} \gtrsim 10^2 M_\odot$.

We can see that the D in Eq. (19) is ~ 1000 times larger than that in eq. (8) of Baumgardt et al. (2004a). Before we discuss about the discrepancy between their and our TDE rates (D), we point out inconsistency between eqs. (7) and (8) of Baumgardt et al. (2004a). When we adopt $k_D = 65$ and $\alpha = 1.55$ in the same way as Baumgardt et al. (2004a), we obtain $D \sim 170 \text{ Gpc}^{-1}$, not $D \sim 11 \text{ Gpc}^{-1}$. Actually, it is unclear which either $k_D = 65$ or eq. (8) is correct (in private communication with H. Baumgardt). Since we find $k_D \sim 30$ from our results, we assume that $k_D = 65$ is correct. In this case, $D \sim 170 \text{ Gpc}^{-1}$ in Baumgardt et al. (2004a). Nevertheless, our D is still ~ 100 times larger than their D .

This discrepancy comes from γ in Eq. (16). Baumgardt et al. (2004a) have chosen $\gamma = 2$ from their simulations (see their fig. 3), while we do $\gamma = 0.3$ from our simulation (see Figure 9). If we

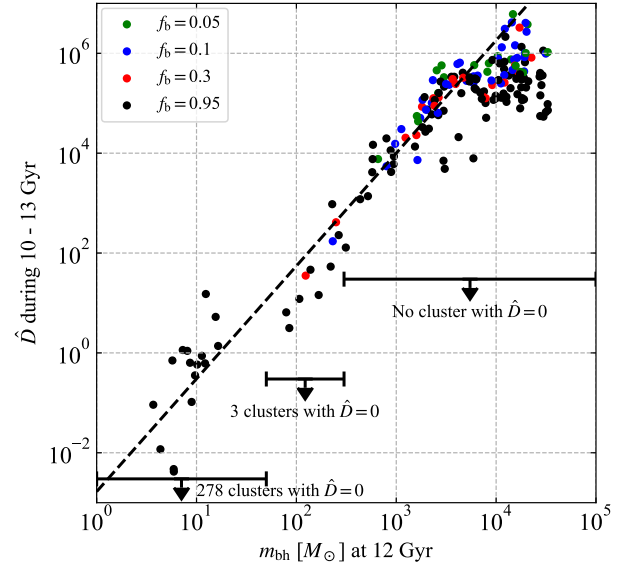


Figure 10. Scaled TDE rates during 10–13 Gyr as a function of the maximum BH mass at 12 Gyr. Clusters with $m_{\text{bh}}/M_{\text{cl}} > 0.5$ are excluded. Color codes indicate the initial binary fraction of a cluster. The dashed line indicate Eq. (20). There are many clusters without WD TDEs during 10–13 Gyr ($\hat{D} = 0$). The presence of these clusters are indicated by arrows with bars. The numbers of such clusters with $m_{\text{bh}} = 1-50$ and $50-300 M_\odot$ are 287 and 3, respectively. There are no clusters with $\hat{D} = 0$ and $m_{\text{bh}} > 300 M_\odot$.

substitute $\gamma = 2$ into Eq. (19), we get $D \sim 57 \text{ Gyr}^{-1}$, which is comparable to their D . This means that our clusters harbor 7 times larger stellar cusps than clusters of Baumgardt et al. (2004a), if the two clusters have the same m_{bh} and v_c . This results indicate that our WD TDE rate agrees with a WD TDE rate of Baumgardt et al. (2004a) if we give the same BHs and stellar cusps. In other words, the loss cone theory holds for both the cases. However, if we give the same BHs and clusters, our WD TDE rate is larger than theirs, since our cluster forms a larger stellar cusp than their cluster. Reasons for this difference are unclear. Their and our simulations contain a lot of different setup: IMFs, stellar evolution models, cluster histories, numerical methods, and so on. We emphasize that no BHs are pinned to the cluster centers in N -body simulations of Baumgardt et al. (2004a) and simulations of MOCCA-SURVEY Database I. Thus in both the simulations BHs experience Brownian motion, which can have great impacts on TDE rates (Magorrian & Tremaine 1999). As a reference, we can obtain $\gamma \sim 0.9$ when we combine Eq. (16) and Eq. (A1) of Stone et al. (2018) under the Bahcall-Wolf cusp, where the latter equation is obtained from an approximate analytic estimate. This value is intermediate between Baumgardt et al. (2004a) and our values. In either case, we need detail comparisons among numerical and analytic models in order to obtain the correct value of γ . We stop finding out the reasons here.

If we prepare a cluster with the same m_{bh} , n_c , and v_c , our WD TDE rate density in the current GCs is 1000 larger than obtained from eq. (8) of Baumgardt et al. (2004a) without correction about inconsistency between eqs. (7) and (8). However, we can also derive m_{bh} , n_c , and v_c from the database. We find that many clusters in the database have $n_c < 10^5 \text{ pc}^{-3}$ and $v_c > 10 \text{ km s}^{-1}$ (see Figure 9, for

example). Thus, our TDE rate in the current GCs is only 100 larger than the previous one.

Our WD TDE rate density in GCs ($\sim 4.5 \times 10^2 \text{ yr}^{-1} \text{ Gpc}^{-3}$) is much larger than the total WD TDE rate density in GCs and dwarf galaxies predicted by MacLeod et al. (2016a) and Maguire et al. (2020). They have estimated the total WD TDE density as $\sim 10 \text{ yr}^{-1} \text{ Gpc}^{-3}$ or $\sim 300 f_{\text{BH}} \text{ yr}^{-1} \text{ Gpc}^{-3}$, where f_{BH} is the BH occupation probability for dwarf galaxies. Here, we adopt $f_{\text{BH}} \sim 0.03$, the lower limit of f_{BH} derived by Reines et al. (2013), Moran et al. (2014), and Baldassare et al. (2018)². Their rate density is dominated by WD TDEs in dwarf galaxies. They have assumed that WD TDEs in a dwarf galaxy with a BH happen 1000 times more efficiently than a GC with a BH. Note that Fragione et al. (2020) have pointed out that WD TDEs can be in triple stellar systems, however its rate density is a fraction of the WD TDE rate density in GCS and dwarf galaxies described above. On the other hand, we find that the WD TDE rate density in the current GCs is 100 larger than those obtained by them, and exceeds the total WD TDE rate density in the current GCs and dwarf galaxies obtained by them. This is because our WD TDE rate in each GC is comparable to their WD TDE rate in each dwarf galaxy, and the current GC number density is 10 – 100 times larger than the current dwarf galaxy number density. When we take into account our WD TDEs in YMCs, and their WD TDEs in dwarf galaxies, we obtain $\sim 5 \times 10^2 \text{ yr}^{-1} \text{ Gpc}^{-3}$ for the WD TDE rate density in the current universe, and the rate density is dominated by GCs. In summary, our WD TDE rate density in the current universe is ~ 50 times larger than predicted previously.

Finally, we remark that we may overestimate the WD TDE rate density, since we overestimate BH growth for the following five reasons. First, in a TDE, a BH should accrete a small fraction of a disrupted star (Shiokawa et al. 2015; Metzger & Stone 2016; Dai et al. 2018; Law-Smith et al. 2019). However, in star cluster models of the database, a BH accretes the whole mass of a disrupted star. Thus, BHs grow in the star cluster models much more than in reality. Second, we do not account for GW recoil kicks induced by BH mergers. They can eject BH merger remnants from the stellar cores and the clusters. They can inhibit BH growth. As described in Appendix C (model C), the WD TDE rate density decreases by about 5 times when the GW recoil kicks are considered. Third, we calculate the WD TDE rate density according to the case I of Eq. (5). On the other hand, the WD TDE rate density decreases by about 5 times when we adopt the case II (see model B in Appendix B). Thus, we overestimate the WD TDE rate by at most 5 times. Fourth, we set the maximum stellar mass to $100 M_{\odot}$ at the initial time. If we adopt a higher value (say $150 M_{\odot}$) for the maximum stellar mass, we get more many BHs. In this case, BHs are more likely to be ejected through few-body interactions among themselves. This also prevents BH growth. As seen in Eq. (19), a TDE rate increases with BH mass increasing. If we overestimate BH mass in a cluster, we also overestimate a WD TDE rate in a cluster. Fifth, we may assume larger GC number density (n_{GC}) than in reality. Since WD TDEs dominate all the WD TDEs in the local universe according to our results, we may overestimate the WD TDE rate density by about 10 times. Therefore, we should keep in mind that the estimated WD TDE rate is the upper limit, i.e. $\lesssim 5 \times 10^2 \text{ yr}^{-1} \text{ Gpc}^{-3}$. When we consider the WD TDE rate density in model C (see Appendix C) as the lower limit, the WD TDE rate can be $90\text{--}500 \text{ yr}^{-1} \text{ Gpc}^{-3}$.

² There are large uncertainties in f_{BH} ; Miller et al. (2015) have suggested its lower limit is ~ 0.2 . Nevertheless, even if $f_{\text{BH}} = 1$, our WD TDE rate density in GCs is larger than the total WD TDE rate density in GCs and dwarf galaxies.

5 DETECTABILITY

We obtain the current WD TDE rate density of $\lesssim 5 \times 10^2 \text{ yr}^{-1} \text{ Gpc}^{-3}$. Most of them is responsible for $10^3 - 10^4 M_{\odot}$ BHs in GCs. Disrupted WDs consist of 2.2 % He WDs, 88 % CO WDs, and 10 % ONe WDs. Based on these results, we discuss about detectability of WD TDEs. We use the same observational parameters as MacLeod et al. (2016a) and Maguire et al. (2020) unless specified otherwise.

WD TDEs can launch luminous jets, which can be detected by wide-field monitors, such as *Swift*'s Burst Alert Telescope (BAT). We assume that such jets have a luminosity of $\sim 10^{48} \text{ erg s}^{-1}$ and a beaming factor of $\sim 1/50$. Then, the BAT can detect the jet up to redshift $z \sim 1$. This means the detectable volume is $\sim 150 \text{ Gpc}^3$. The BAT can cover 20 % of the sky. We put them together, and obtain the detection rate of the BAT as $\lesssim 300 \text{ yr}^{-1}$. This may not be consistent with the detection rate of gamma-ray bursts by the BAT, $\lesssim 100 \text{ yr}^{-1}$. Moreover, ultra-long gamma-ray bursts, one of possible EM counterparts of WD TDEs (e.g. Ioka et al. 2016), occupy a small fraction of all gamma-ray bursts. There may be two reasons for this inconsistency. First, we may overestimate the WD TDE rate density as summarized in the final part of section 4. Second, WD TDEs generate luminous jets less efficiently than expected. For example, the beaming factor of TDEs can be 0.1 (Zauderer et al. 2011; Cenko et al. 2012). WD TDEs may have to satisfy special conditions for jet launching, similarly to MS TDEs (van Velzen et al. 2013; Bower et al. 2013; Genzorov et al. 2017).

A part of WD TDEs can trigger thermonuclear explosion of disrupted WDs, and can be observed similarly to SNe Ia. Hereafter, we call this “thermonuclear transients”. The LSST will be the most powerful to search for such thermonuclear transients in the near future. If a $0.6 M_{\odot}$ CO WD experiences such thermonuclear explosion, the LSST can detect it within a volume of 13.3 Gpc^3 . The LSST has a sky coverage of ~ 0.5 . We suppose that 1/6 of WD TDEs can have thermonuclear explosion. Then, the detection rate is $\lesssim 550 \text{ yr}^{-1}$.

This detection rate is based on a WD TDE with a $0.6 M_{\odot}$ CO WD disrupted by a $10^3 M_{\odot}$ BH. However, luminosity of a thermonuclear transient depends on WD mass (MacLeod et al. 2016a; Kawana et al. 2020). Moreover, the success rate of thermonuclear explosion should be sensitive to both BH and WD masses, and WD compositions (e.g. Rosswog et al. 2009a; Kawana et al. 2018; Anninos et al. 2018). As seen in Figure 3, WD mass ranges from $0.5 M_{\odot}$ to $1.4 M_{\odot}$ in a nearly uniform way, and BH mass can be $10^3 - 10^4 M_{\odot}$ with the same probability. We should keep in mind that the detection rate contains uncertainties due to different BH and WD masses.

Thermonuclear transients will be helpful to identify WD TDEs. We discuss about how they are observed. There are two previous studies to investigate emission properties of such transients. MacLeod et al. (2016a) have examined a TDE of a $0.6 M_{\odot}$ CO WD, while Kawana et al. (2020) have focused on a TDE of a $0.2 M_{\odot}$ He WD. Both of them have suggested that such transients should be rapid and faint transients in optical and ultraviolet bands. Their evolution timescale is ~ 10 days, which is shorter than SNe Ia (~ 20 days). This is because their photon diffusion timescale is shorter due to their smaller total mass ($\sim 0.1 - 0.5 M_{\odot}$) than SNe Ia ($\sim 1.0 - 1.5 M_{\odot}$). Their absolute magnitude is $\lesssim -18$, which is fainter than SNe Ia ($\sim -19 - -20$). They yield only $\lesssim 0.1 M_{\odot}$ of radioactive nuclei, such as ^{56}Ni , while SNe Ia have ^{56}Ni of $\sim 0.6 M_{\odot}$.

However, these results may not apply for a significant fraction of WD TDEs. As seen in Figure 3, 20 % of WD TDEs contain $\geq 1.0 M_{\odot}$ WDs. Such WD TDEs have long evolution timescale, similar to SNe Ia. If they yield a large amount of ^{56}Ni , even their light curves can resemble those of SNe Ia. In this case, we need not only photometric

observations but also spectroscopic observations in order to identify WD TDEs. WD TDEs can have Doppler shift of their spectral lines up to $\sim 10,000 \text{ km s}^{-1}$ due to their orbital motion around BHs (MacLeod et al. 2016a; Kawana et al. 2020). Half of $\geq 1.0 M_{\odot}$ WDs (or 10 % of all WDs) are ONe WDs. It should be instructive to investigate how ONe WD TDEs are observed.

WD TDEs can be GW transients. LISA can detect only WD TDEs in the local group (Rosswog et al. 2009a; Anninos et al. 2018), since the LISA band is different from GW frequency of WD TDEs. Thus, the detection rate is extremely low, $\lesssim 10^{-5} \text{ yr}^{-1}$. On the other hand, GW observatories sensitive to decihertz GWs, such as DECIGO, can discover WD TDEs even in the high-redshift universe (Arca Sedda et al. 2020).

Zhang et al. (2017) have claimed that jets associated with ONe WD TDEs can be sources of ultra high-energy cosmic rays. This model requires a ONe WD TDE rate of 0.1 and $10 \text{ yr}^{-1} \text{ Gpc}^{-3}$ (Alves Batista & Silk 2017; Biehl et al. 2018, respectively), depending on the baryon loading of the jets. Our ONe WD TDE rate is $\lesssim 50 \text{ yr}^{-1} \text{ Gpc}^{-3}$, large enough for this model. However, our CO WD TDE rate density is ~ 10 times larger than our ONe WD TDE rate. Thus, our WD TDE rate density may not be consistent with this model, unless there are some processes to prevent CO WD TDEs from yielding ultra high-energy cosmic rays.

Finally, we mention multiple TDEs with at least one WD TDE. The fraction of such multiple TDEs to the total WD TDEs is only ~ 2 %. However, they are quite interesting, since they have distinct features owing to multiple emission components. Conversely, if an MS TDE is found, it is worth examining the presence of a hidden WD TDE. The discovery of such a hidden WD TDE will make the presence of an IMBH conclusive.

6 SUMMARY

We have investigated MOCCA-SURVEY Database I, and obtain the local rate density of WD TDEs in GCs and YMCs. The large data enables us to calculate not only the total rate density, but also its derivatives. We have found that the local rate density including WD TDEs in dwarf galaxies is $\sim 90\text{--}500 \text{ yr}^{-1} \text{ Gpc}^{-3}$ in model A, 90 % of which are WD TDEs in GCs. This rate density is 9–50 times larger than predicted by MacLeod et al. (2016a) and Maguire et al. (2020). WD TDEs in our cluster models happen 200–1000 times more efficiently than in cluster models of Baumgardt et al. (2004a), used by MacLeod et al. (2016a) and Maguire et al. (2020). This is because our cluster models have 7 times larger stellar cusps than Baumgardt’s models, even if their and our cluster models have the same cluster cores. Our results may increase the detectability of luminous jets, X-ray flares, and thermonuclear transients induced by WD TDEs by 9–50 times, compared with previous estimates. However, we have to make a caveat that we may overestimate the WD TDE rate density because of inconsistency in the mass growth of IMBHs as discussed in section 4.

We have also found that 20 % of disrupted WDs have $\geq 1.0 M_{\odot}$, and half of them are ONe WDs. If they experience thermonuclear explosions, they can be observed as luminously and long as SNe Ia. This is different from previous expectations that thermonuclear transients should be more rapid and faint than SNe Ia because of smaller ejecta masses and radioactive masses (MacLeod et al. 2016a; Kawana et al. 2020). Our results indicate that we need to investigate observational features of massive WD TDEs.

The rate density of ONe WD TDEs is $\lesssim 50 \text{ yr}^{-1} \text{ Gpc}^{-3}$, large enough to yield observed ultra high-energy cosmic rays. However,

CO WD TDEs happens 8 times more frequently than ONe WD TDEs. If WD TDEs are the origin of ultra high-energy cosmic rays, CO WD TDEs may need not to create ultra high-energy cosmic rays.

ACKNOWLEDGMENTS

We are very grateful to the anonymous referee for many constructive suggestions. AT thanks A. Askar, H. Baumgardt, G. Fragione, K. Kawana, M. MacLeod, and Y. Suwa for fruitful discussions. AT was supported in part by Grants-in-Aid for Scientific Research (17H06360, 19K03907) from the Japan Society for the Promotion of Science. MG was partially supported by the Polish National Science Center (NCN) through the grant UMO-2016/23/B/ST9/02732. MAS acknowledges financial support from the Alexander von Humboldt Foundation for the research program “The evolution of black holes from stellar to galactic scales”, the Volkswagen Foundation Trilateral Partnership through project No. I/97778 “Dynamical Mechanisms of Accretion in Galactic Nuclei”, and the Deutsche Forschungsgemeinschaft (DFG, German Research Foundation) – Project-ID 138713538 – SFB 881 “The Milky Way System”, and funding from the European Union’s Horizon 2020 research and innovation programme under the Marie Skłodowska-Curie grant agreement No. 101025436 (project GRACE-BH, PI Manuel Arca Sedda).

DATA AVAILABILITY

The data underlying this article can be obtained upon request to Mirek Giersz (mig@camk.edu.pl) and after agreeing to the terms of the MOCCA License. The license can be found in <https://moccacode.net/license/>.

REFERENCES

- Abbott R., et al., 2020a, *Phys. Rev. Lett.*, **125**, 101102
- Abbott R., et al., 2020b, *ApJ*, **900**, L13
- Acernese F., et al., 2015, *Classical and Quantum Gravity*, **32**, 024001
- Alves Batista R., Silk J., 2017, *Phys. Rev. D*, **96**, 103003
- Amaro-Seoane P., et al., 2017, arXiv e-prints, p. arXiv:1702.00786
- Anninos P., Fragile P. C., Olivier S. S., Hoffman R., Mishra B., Camarda K., 2018, *ApJ*, **865**, 3
- Anninos P., Hoffman R. D., Grewal M., Lavell M. J., Fragile P. C., 2019, *ApJ*, **885**, 136
- Arca-Sedda M., Capuzzo-Dolcetta R., 2014, *ApJ*, **785**, 51
- Arca Sedda M., Askar A., Giersz M., 2018, *MNRAS*, **479**, 4652
- Arca Sedda M., Askar A., Giersz M., 2019, arXiv e-prints, p. arXiv:1905.00902
- Arca Sedda M., et al., 2020, *Classical and Quantum Gravity*, **37**, 215011
- Askar A., Szkudlarek M., Gondek-Rosińska D., Giersz M., Bulik T., 2017a, *MNRAS*, **464**, L36
- Askar A., Bianchini P., de Vita R., Giersz M., Hypki A., Kamann S., 2017b, *MNRAS*, **464**, 3090
- Askar A., Arca Sedda M., Giersz M., 2018, *MNRAS*, **478**, 1844
- Bahcall J. N., Wolf R. A., 1976, *ApJ*, **209**, 214
- Baldassare V. F., Geha M., Greene J., 2018, *ApJ*, **868**, 152
- Baumgardt H., Makino J., Ebisuzaki T., 2004a, *ApJ*, **613**, 1143
- Baumgardt H., Makino J., Ebisuzaki T., 2004b, *ApJ*, **613**, 1133
- Behroozi P. S., Wechsler R. H., Conroy C., 2013, *ApJ*, **770**, 57
- Belczynski K., Kalogera V., Bulik T., 2002, *ApJ*, **572**, 407
- Belloni D., Giersz M., Askar A., Leigh N., Hypki A., 2016, *MNRAS*, **462**, 2950
- Belloni D., Giersz M., Rocha-Pinto H. J., Leigh N. W. C., Askar A., 2017, *MNRAS*, **464**, 4077

- Belloni D., Kroupa P., Rocha-Pinto H. J., Giersz M., 2018, *MNRAS*, **474**, 3740
- Belloni D., Giersz M., Rivera Sandoval L. E., Askar A., Ciecieląg P., 2019, *MNRAS*, **483**, 315
- Biehl D., Boncioli D., Lunardini C., Winter W., 2018, *Scientific Reports*, **8**, 10828
- Bower G. C., Metzger B. D., Cenko S. B., Silverman J. M., Bloom J. S., 2013, *ApJ*, **763**, 84
- Bulik T., Belczyński K., Rudak B., 2004, *A&A*, **415**, 407
- Capuzzo-Dolcetta R., 1993, *ApJ*, **415**, 616
- Cenko S. B., et al., 2012, *ApJ*, **753**, 77
- Clausen D., Eracleous M., 2011, *ApJ*, **726**, 34
- Dai L., McKinney J. C., Roth N., Ramirez-Ruiz E., Miller M. C., 2018, *ApJ*, **859**, L20
- Ebisuzaki T., et al., 2001, *ApJ*, **562**, L19
- Farrell S. A., Webb N. A., Barret D., Godet O., Rodrigues J. M., 2009, *Nature*, **460**, 73
- Ferrarese L., Merritt D., 2000, *ApJ*, **539**, L9
- Fragione G., Metzger B. D., Perna R., Leigh N. W. C., Kocsis B., 2020, *MNRAS*, **495**, 1061
- Frank J., Rees M. J., 1976, *MNRAS*, **176**, 633
- Fregeau J. M., Cheung P., Portegies Zwart S. F., Rasio F. A., 2004, *MNRAS*, **352**, 1
- Fukushige T., Heggie D. C., 2000, *MNRAS*, **318**, 753
- Generozov A., Mimica P., Metzger B. D., Stone N. C., Giannios D., Aloy M. A., 2017, *MNRAS*, **464**, 2481
- Giersz M., Heggie D. C., Hurley J. R., 2008, *MNRAS*, **388**, 429
- Giersz M., Heggie D. C., Hurley J. R., Hypki A., 2013, *MNRAS*, **431**, 2184
- Giersz M., Leigh N., Hypki A., Lützgendorf N., Askar A., 2015, *MNRAS*, **454**, 3150
- Giersz M., Askar A., Klencki J., Morawski J., 2019a, arXiv e-prints, p. arXiv:1904.03591
- Giersz M., Askar A., Wang L., Hypki A., Leveque A., Spurzem R., 2019b, *MNRAS*, **487**, 2412
- Gnedin O. Y., Ostriker J. P., Tremaine S., 2014, *ApJ*, **785**, 71
- Guillochon J., Manukian H., Ramirez-Ruiz E., 2014, *ApJ*, **783**, 23
- Hénon M. H., 1971, *Ap&SS*, **14**, 151
- Hobbs G., Lorimer D. R., Lyne A. G., Kramer M., 2005, *MNRAS*, **360**, 974
- Hong J., Askar A., Giersz M., Hypki A., Yoon S.-J., 2020, *MNRAS*, **498**, 4287
- Hurley J. R., Pols O. R., Tout C. A., 2000, *MNRAS*, **315**, 543
- Hurley J. R., Tout C. A., Pols O. R., 2002, *MNRAS*, **329**, 897
- Ioka K., Hotokezaka K., Piran T., 2016, *ApJ*, **833**, 110
- Ivezic Z., et al., 2019, *ApJ*, **873**, 111
- Jonker P. G., et al., 2012, *ApJ*, **758**, 28
- Jonker P. G., et al., 2013, *ApJ*, **779**, 14
- Kagra Collaboration et al., 2019, *Nature Astronomy*, **3**, 35
- Katz H., Ricotti M., 2013, *MNRAS*, **432**, 3250
- Kawamura S., et al., 2011, *Classical and Quantum Gravity*, **28**, 094011
- Kawana K., Tanikawa A., Yoshida N., 2018, *MNRAS*, **477**, 3449
- Kawana K., Maeda K., Yoshida N., Tanikawa A., 2020, *ApJ*, **890**, L26
- King I. R., 1966, *AJ*, **71**, 64
- Komossa S., 2015, *Journal of High Energy Astrophysics*, **7**, 148
- Kormendy J., Ho L. C., 2013, *ARA&A*, **51**, 511
- Kormendy J., Richstone D., 1995, *ARA&A*, **33**, 581
- Krolik J. H., Piran T., 2011, *ApJ*, **743**, 134
- Kroupa P., 2001, *MNRAS*, **322**, 231
- Krumholz M. R., McKee C. F., Bland-Hawthorn J., 2019, *ARA&A*, **57**, 227
- Kuin N. P. M., et al., 2019, *MNRAS*, **487**, 2505
- LIGO Scientific Collaboration et al., 2015, *Classical and Quantum Gravity*, **32**, 074001
- Law-Smith J., Guillochon J., Ramirez-Ruiz E., 2019, *ApJ*, **882**, L25
- Leigh N. W. C., Giersz M., Marks M., Webb J. J., Hypki A., Heinke C. O., Kroupa P., Sills A., 2015, *MNRAS*, **446**, 226
- Levan A. J., et al., 2014, *ApJ*, **781**, 13
- Leveque A., Giersz M., Paolillo M., 2021, *MNRAS*, **501**, 5212
- Lu W., Bonnerot C., 2020, *MNRAS*, **492**, 686
- Luminet J.-P., Pichon B., 1989, *A&A*, **209**, 103
- MacLeod M., Goldstein J., Ramirez-Ruiz E., Guillochon J., Samsing J., 2014, *ApJ*, **794**, 9
- MacLeod M., Guillochon J., Ramirez-Ruiz E., Kasen D., Rosswog S., 2016a, *ApJ*, **819**, 3
- MacLeod M., Trenti M., Ramirez-Ruiz E., 2016b, *ApJ*, **819**, 70
- Madau P., Fragos T., 2017, *ApJ*, **840**, 39
- Magorrian J., Tremaine S., 1999, *MNRAS*, **309**, 447
- Magorrian J., et al., 1998, *AJ*, **115**, 2285
- Maguire K., Eracleous M., Jonker P. G., MacLeod M., Rosswog S., 2020, *Space Sci. Rev.*, **216**, 39
- Matsumoto H., Tsuru T. G., Koyama K., Awaki H., Canizares C. R., Kawai N., Matsushita S., Kawabe R., 2001, *ApJ*, **547**, L25
- Metzger B. D., Stone N. C., 2016, *MNRAS*, **461**, 948
- Miller B. P., Gallo E., Greene J. E., Kelly B. C., Treu T., Woo J.-H., Baldassare V., 2015, *ApJ*, **799**, 98
- Moran E. C., Shahinyan K., Sugarman H. R., Vélez D. O., Eracleous M., 2014, *AJ*, **148**, 136
- Morawski J., Giersz M., Askar A., Belczynski K., 2018, *MNRAS*, **481**, 2168
- Mueller G., et al., 2019, in Bulletin of the American Astronomical Society, p. 243 (arXiv:1907.11305)
- Portegies Zwart S. F., McMillan S. L. W., 2000, *ApJ*, **528**, L17
- Portegies Zwart S. F., Baumgardt H., Hut P., Makino J., McMillan S. L. W., 2004, *Nature*, **428**, 724
- Portegies Zwart S. F., McMillan S. L. W., Gieles M., 2010, *ARA&A*, **48**, 431
- Prentice S. J., et al., 2018, *ApJ*, **865**, L3
- Rees M. J., 1984, *ARA&A*, **22**, 471
- Reines A. E., Greene J. E., Geha M., 2013, *ApJ*, **775**, 116
- Rodriguez C. L., Haster C.-J., Chatterjee S., Kalogera V., Rasio F. A., 2016, *ApJ*, **824**, L8
- Rossi E. M., Stone N. C., Law-Smith J. A. P., MacLeod M., Lodato G., Dai J. L., Mandel I., 2020, arXiv e-prints, p. arXiv:2005.12528
- Rosswog S., Ramirez-Ruiz E., Hix W. R., Dan M., 2008, *Computer Physics Communications*, **179**, 184
- Rosswog S., Ramirez-Ruiz E., Hix W. R., 2009a, *ApJ*, **695**, 404
- Rosswog S., Kasen D., Guillochon J., Ramirez-Ruiz E., 2009b, *ApJ*, **705**, L128
- Samsing J., Askar A., Giersz M., 2018, *ApJ*, **855**, 124
- Sell P. H., Maccarone T. J., Kotak R., Knigge C., Sand D. J., 2015, *MNRAS*, **450**, 4198
- Sell P. H., Arur K., Maccarone T. J., Kotak R., Knigge C., Sand D. J., Valenti S., 2018, *MNRAS*, **475**, L111
- Sesana A., Vecchio A., Eracleous M., Sigurdsson S., 2008, *MNRAS*, **391**, 718
- Shen R.-F., 2019, *ApJ*, **871**, L17
- Shiokawa H., Krolik J. H., Cheng R. M., Piran T., Noble S. C., 2015, *ApJ*, **804**, 85
- Stodolkiewicz J. S., 1986, *Acta Astron.*, **36**, 19
- Stone N. C., Küpper A. H. W., Ostriker J. P., 2017, *MNRAS*, **467**, 4180
- Stone N. C., Generozov A., Vasiliev E., Metzger B. D., 2018, *MNRAS*, **480**, 5060
- Stone N. C., Kesden M., Cheng R. M., van Velzen S., 2019, *General Relativity and Gravitation*, **51**, 30
- Takekawa S., Oka T., Iwata Y., Tsujimoto S., Nomura M., 2019, *ApJ*, **871**, L1
- Takekawa S., Oka T., Iwata Y., Tsujimoto S., Nomura M., 2020, *ApJ*, **890**, 167
- Tanaka K., 2018, *ApJ*, **859**, 86
- Tanaka K., Oka T., Matsumura S., Nagai M., Kamegai K., 2014, *ApJ*, **783**, 62
- Tanikawa A., 2018a, *MNRAS*, **475**, L67
- Tanikawa A., 2018b, *ApJ*, **858**, 26
- Tanikawa A., Sato Y., Nomoto K., Maeda K., Nakasato N., Hachisu I., 2017, *ApJ*, **839**, 81
- Thorne K. S., Zytlow A. N., 1975, *ApJ*, **199**, L19
- Tremaine S. D., Ostriker J. P., Spitzer L. J., 1975, *ApJ*, **196**, 407
- Volonteri M., 2012, *Science*, **337**, 544
- Zauderer B. A., et al., 2011, *Nature*, **476**, 425
- Zhang B. T., Murase K., Oikonomou F., Li Z., 2017, *Phys. Rev. D*, **96**, 063007
- van Velzen S., Frail D. A., Kording E., Falcke H., 2013, *A&A*, **552**, A5

APPENDIX A: OTHER TDES

In this section, we focus on other TDEs than WD TDEs, in particular MS TDEs. Figure A1 shows the MS TDE rates during 10 – 13 Gyr as a function of the maximum BH mass at 12 Gyr. The left and right panels indicate MS TDE rates calculated in model A and B in Eq. (5), respectively. MS TDE rates in model A are larger than in model B by an order of magnitude for $m_{\text{bh}} \gtrsim 10^3 M_{\odot}$. This is because the tidal radii of MSs are larger than the stellar radii of MSs.

Figure A2 shows the scaled MS TDE rates during 10 – 13 Gyr as a function of the maximum BH mass at 12 Gyr in model A (left) and model B (right). The scaled MS TDE rates calculated in model B does not fit to Eq. (20). On the other hand, the scaled MS TDE rates calculated in model A match well with Eq. (20), similarly to the scaled WD TDE rates (see Figure 10).

Figure A3 shows the MS, PMS, and HeS TDE rate densities calculated in model A (left) and model B (right). The MS TDE rate density is much larger than other TDE rate densities including the WD TDE rate density regardless of the choice of models A and B. YMCs contribute to these TDEs more than GCs. Thus, the BH mass distribution has a peak at $\sim 10^3 M_{\odot}$ in contrary to that of WD TDEs. Note that BHs in YMCs can not grow up to $\sim 10^4 M_{\odot}$, since YMCs have smaller mass than GCs at the initial time. YMCs contain young massive stars, and thus the mass distribution of disrupted stars has a peak at $2 - 3 M_{\odot}$. Owing to the presence of such massive stars, these TDE rate densities in YMCs exceed those in GCs in model B. The tendency described above is not sensitive to models A and B.

APPENDIX B: NON-CORRECTED WD TDE RATE

In this section, we show the WD TDE rate calculated in model B. Figure B1 corresponds to Figure 3. The total WD TDE rate density in model B is about 5 times smaller than in model A. The corrective factor C_{tde} in the case I of Eq. (5) is larger than unity, since $d_{\text{tde}}/d_{\text{coal}}$ is larger than unity as seen in Figure 2. Nevertheless, the total WD TDE rate density is larger than estimated previously ($\sim 10 \text{ yr}^{-1} \text{ Gpc}^{-3}$) by an order of magnitude. The BH mass distribution has a peak at a few $10^3 M_{\odot}$ in model A, while the peak shifts to $\sim 10^4 M_{\odot}$ in model B. This is because the corrective factor C_{tde} takes the maximum at a few $10^3 M_{\odot}$ (see Figure 2). Thus, our conclusion that IMBHs dominate WD TDEs is robust. The WD mass distribution in model B becomes more flat than in model A in the range between 0.5 and $1.4 M_{\odot}$. This reason is that $d_{\text{tde}}/d_{\text{coal}}$ becomes larger for smaller WD mass. The contribution of ONe WDs is significant even in model A, and is more pronounced in model B.

Figure B2 shows the scaled WD TDE rates in model B, corresponding to Figure 10 in model A. Because C_{tde} is larger than unity in the case I of Eq. (5), the scaled WD TDE rates in model B are smaller than in model A. Thus, the rates deviate from Eq. (20) downward. Nevertheless, the deviation is small, a factor of about 5, and the dependence on m_{bh} is similar to Eq. (20) over several orders of magnitude of m_{bh} . The theory deducing Eq. (20) should be correct, and Eq. (20) would be still helpful to estimate WD TDE rates in star clusters.

APPENDIX C: PESSIMISTIC CASE

Here, we show WD TDEs in model C. In this model, we consider the pessimistic case for IMBH formation. Before we explain the pessimistic case, we describe the IMBH formation mechanisms.

Giersz et al. (2015) have found that IMBHs can grow in either of two ways, the so-called fast and slow scenarios. In the fast scenario, IMBHs appear through mergers of stellar-mass BHs and massive stars, where such massive stars are formed through runaway mergers. Since this scenario needs massive stars, it happens only in a young phase of a cluster. In the slow scenario, a $\sim 100 M_{\odot}$ BH is built up by mergers of stellar-mass BHs and NSs, and grows through coalescences with low-mass stars. Since the building up happens after gravothermal core collapse, the IMBH appears only after a cluster age of about 1 Gyr.

Cluster simulations in MOCCA SURVEY Database I may overestimate and overproduce IMBHs for different reasons between the fast and slow scenarios. For the fast scenario, the cluster simulations assume that stellar-mass BHs perfectly accrete massive stars through their mergers. However, this assumption may overestimate IMBH masses. For the slow scenario, the cluster simulations do not consider GW recoil kicks after BH mergers. Thus, the building up may overproduce IMBHs. In fact, a part of IMBHs fail to grow due to ejections of BHs and NSs through GW recoil kicks (Morawski et al. 2018).

In the pessimistic case, we divide IMBHs into those formed through the fast and slow scenarios according to the time when BHs grow to $150 M_{\odot}$. If the time is less than 300 Myr, IMBHs grow through the fast scenario, and otherwise through the slow scenario (Arca Sedda et al. 2019). We exclude all the WD TDEs driven by IMBHs formed through the fast scenario. This is because the accretion efficiency of massive stars onto stellar-mass BHs may be quite small. We ignore the presence of IMBHs with the probability of 60, 70, and 90 % for clusters with $R_t/R_h = 50, 25$ and 1 (filling), respectively (see Table 1) according to the overall retention fractions shown in table 2 of Morawski et al. (2018).

We generate 21 realizations, because IMBHs formed through the slow scenario survive inside clusters in a stochastic way. Among the 21 realizations, the minimum, median, and maximum values of WD TDE rate densities are 2.3×10^1 , 8.9×10^1 , and $1.8 \times 10^2 \text{ yr}^{-1} \text{ Gpc}^{-3}$, respectively. For $f_{\text{BH,GC}}$, the minimum, median, and maximum values are 0.011, 0.019, and 0.026, respectively. The WD TDE rate densities are weakly correlated with $f_{\text{BH,GC}}$. The WD TDE rate density in model C is typically less than in model A only by about 5 times, despite that $f_{\text{BH,GC}}$ decreases by about 10 times. This is because underfilling clusters (those with $R_t/R_h = 25$ and 50) are easier to retain IMBHs and generate WD TDEs.

Figure C1 shows the WD TDE rate density and its breakdowns for the realization with the median WD TDE rate density among the 21 realizations. The striking feature is the absence of IMBHs with $\sim 10^4 M_{\odot}$. Since such IMBHs are formed through the fast scenario, they cannot contribute to the WD TDE rate density in model C. Other IMBHs can survive inside clusters with a probability described above. Thus, the WD TDE rate density also decreases in IMBHs with $< 10^4 M_{\odot}$. The shape of the WD mass distribution is similar to that in the optimistic case.

This paper has been typeset from a \LaTeX file prepared by the author.

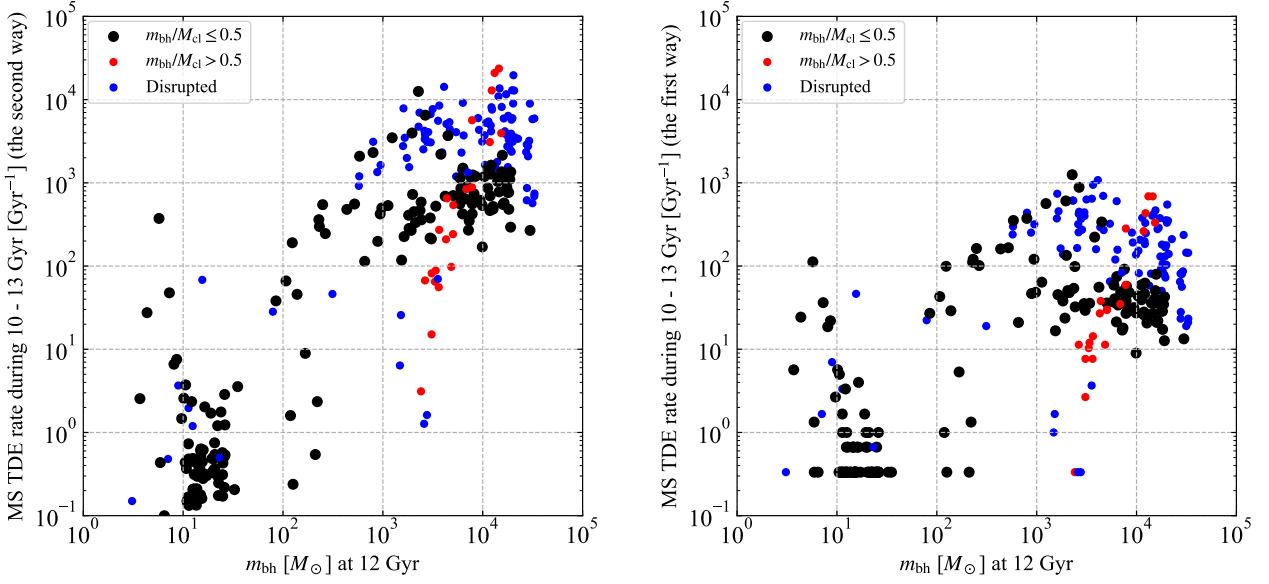


Figure A1. MS TDE rates during 10 – 13 Gyr as a function of the maximum BH mass at 12 Gyr in model A (left) and model B (right). Black and red circles indicate clusters with BH masses $m_{bh}/M_{cl} \leq 0.5$ and > 0.5 , respectively. Blue circles indicate clusters falling into galactic centers at 12 Gyr, or clusters which are not disrupted at 10 Gyr, but disrupted until 12 Gyr.

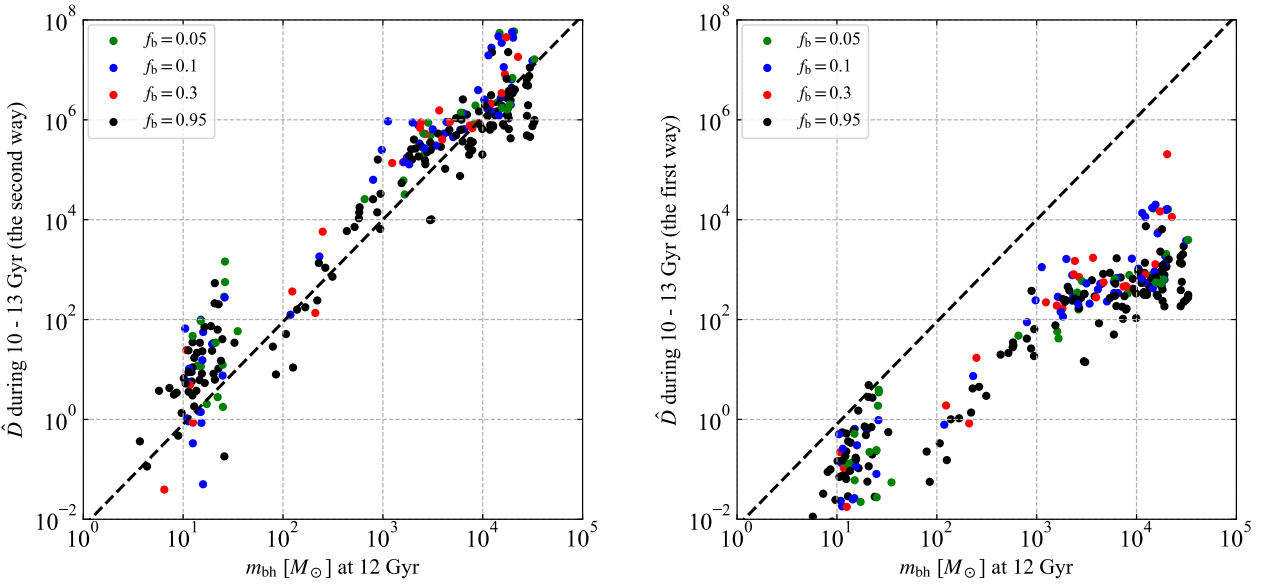


Figure A2. Scaled MS TDE rates during 10 – 13 Gyr as a function of the maximum BH mass at 12 Gyr in model A (left) and model B (right). Color codes and dashed lines are the same as Figures 10.

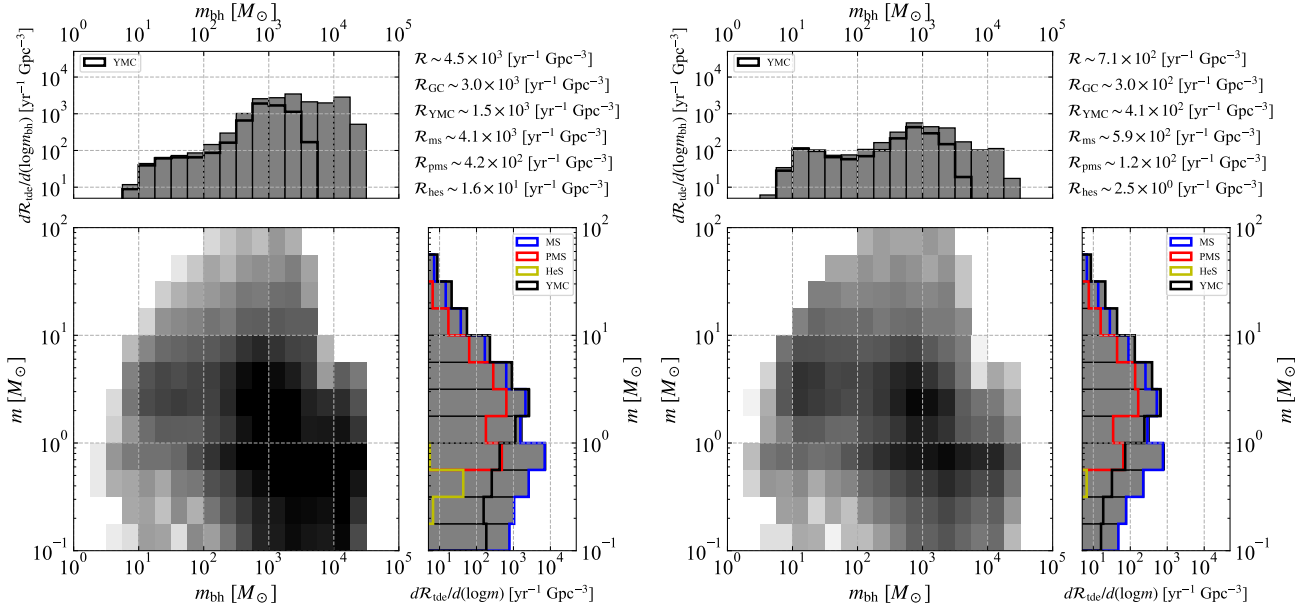


Figure A3. MS, PMS, and HeS TDE rate densities in the current GCs and YMCs calculated in model A (left) and model B (right). Since the left and right figures are the same except for the corrective factors, we only explain the left figure in the following. On the top-right corner, we show the rate densities of all MS, PMS, and HeS TDEs (\mathcal{R}), these TDEs in GCs (\mathcal{R}_{GC}), these TDEs in YMCs (\mathcal{R}_{YMC}), MS TDEs (\mathcal{R}_{ms}), PMS TDEs (\mathcal{R}_{pms}), and HeS TDEs (\mathcal{R}_{hes}). Bottom left: Relative abundance of the rate density per dex stellar mass (m) per dex of m_{bh} in a logarithmic color scale. Top left: The rate density per dex of m_{bh} . Gray-filled histograms indicate all the MS, PMS, and HeS TDEs, and black-open histograms these TDEs only in YMCs. Bottom right: The rate density per dex stellar mass (m). Gray-filled and black-open histograms are the same as in the top left panel. Blue-, red-, and yellow-open histograms indicate MS, PMS, and HeS TDEs, respectively.

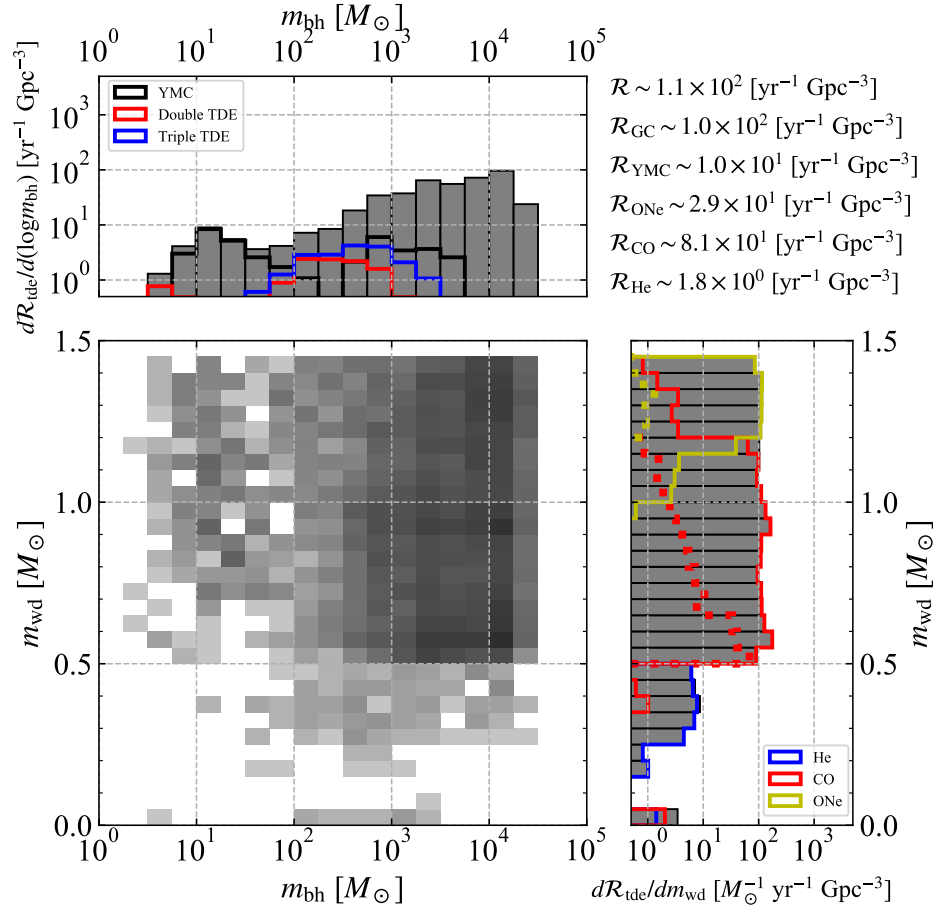


Figure B1. The same as Figure 3, except for model B.

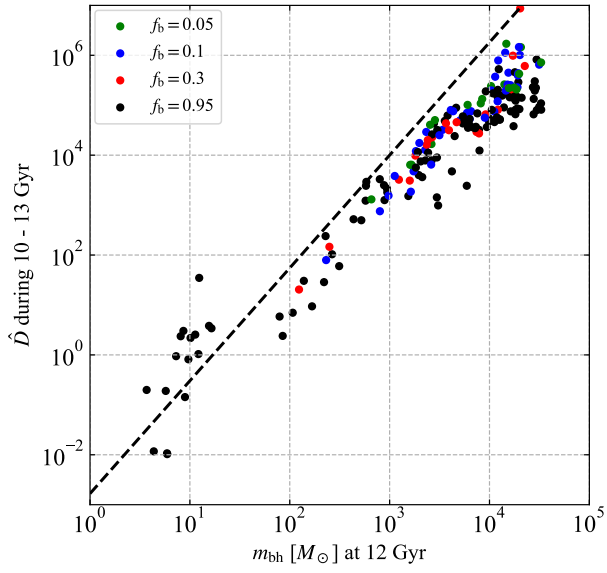


Figure B2. The same as Figure 10, except for model B.

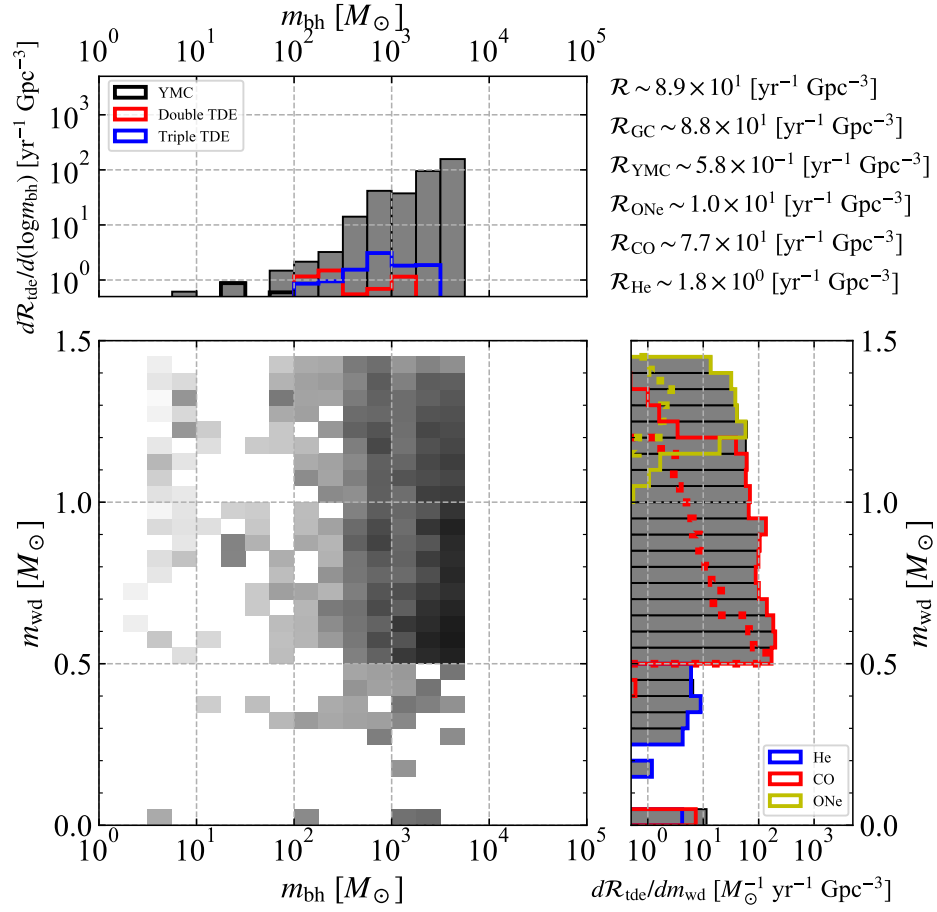


Figure C1. The same as Figure 3, except for a realization in model C. The realization has the median value of WD TDE rate densities among the 21 realizations.